AN INVESTIGATIVE STUDY OF GURNEY FLAPS ON A NACA 0036 AIRFOIL

A Thesis

presented to

the Faculty of California Polytechnic State University,

San Luis Obispo

In Partial Fulfillment

Of the Requirements for the Degree

Master of Science in Aerospace Engineering

by

Greg F. Altmann

March 2011

COMMITTEE MEMBERSHIP

TITLE:	INVESTIGATIVE STUDY OF GURNEY FLAPS ON A NACA 0036 AIRFOIL
AUTHOR:	Greg F. Altmann
DATE SUBMITTED:	February 2011
COMMITTEE CHAIR:	Dr. Jin Tso Advisor and Committee Chair Aerospace Engineering Dept.
COMMITTEE MEMBER:	Dr. Tina Jameson Committee Member Aerospace Engineering Dept.
COMMITTEE MEMBER:	Dr. David D. Marshall Committee Member Aerospace Engineering Dept.
COMMITTEE MEMBER:	Dr. Chee Tung Committee Member NASA Ames

ABSTRACT

Investigative Study of Gurney Flaps on a NACA 0036 Airfoil

Greg F. Altmann

This project examined the effect of Gurney flaps on a 2D, 2-ft chord NACA 0036 airfoil in the Cal Poly 3'x4' low speed wind tunnel at 25 m/s. It also covered the numerical simulation of the experiment in computational fluid dynamics (CFD). During the study, problems with the wind tunnel data were seen. After a careful diagnosis, the problem was traced to dirty flow conditioners which were subsequently replaced.

Five Gurney flaps at 1, 2, 3, 4, and 5% of the chord were tested. The Gurney flaps had the effect of eliminating the lift reversal effect and lowering the profile drag at low angles of attack, ranging from 4-27%. The optimal Gurney flap appeared to be 2% of the chord. CFD modeling of the problem had limited success, with the best results coming from Mentor's k-w SST turbulence model. This model reproduced the non-linear lift curve, and captured the trend in rising drag fairly well, but failed to predict the correct point of separation. Attempts to model the Gurney flap in CFD were unsuccessful.

ACKNOWLEDGEMENTS

I would first like to thank Joshua Roepke for his support through this project. Throughout our partnership with first FSAE and then the wind tunnel, his assistance has been invaluable to help me become a better test engineer. I question how I would have ever solved my wind tunnel problems without his help. I would like to thank my advisor, Dr. Tso, for being readily available and devoting countless hours to the project. I also want to thank my college roommates, and over the last few months, my uncle, for helping me escape the stressful world of my thesis. Thanks to The Boeing Company for letting me see a light at the end of the (wind) tunnel, and getting me to wrap up the project in a timely manner for employment. And, finally, I thank my family for the support and encouragement that they provided and that prompted me to get this task accomplished.

Table of Contents

List of Tables

List of Figures

NOMEMCLATURE

English Symbols

Symbol	Definition
A	Area
c	Chord
C_a	Axial force coefficient
C_d	Sectional drag coefficient, $\frac{d}{q_\infty c}$
C_f	Friction coefficient
C_l	Sectional lift coefficient , $\frac{l}{q_\infty c}$
C_n	Normal force coefficient
C_p	Pressure coefficient, $\frac{p-p_\infty}{q_\infty}$
C_{p_∞}	Tunnel static pressure coefficient
C_q	Tunnel dynamic pressure coefficient
g	Gravitational force
H	Shape factor
K	Pressure drop coefficient
$\bar{k}$	Turbulent kinetic energy
q	Dynamic pressure, $\frac{1}{2}\rho U_\infty^2$
R_e	Reynolds number, $\frac{\rho U_\infty c}{\mu}$
R_{e_k}	Non-dimensional roughness height, $\frac{u_k k}{\nu_k}$
r	Ratio
t	Time
U	Freestream velocity
x	Distance
y^+	Non-dimensional wall distance, $\frac{u_* y}{\nu}$

Greek Symbols

Symbol	Definition
α	Angle of attack
β	Open ratio
θ	Momentum thickness
μ	Dynamic viscosity
ν	Kinematic viscosity
ρ	Density
τ	Shear stress
ϕ	Value of interest

Foreword

Many challenges and hurdles are always encountered in graduate level thesis work. The scope of the current thesis was to investigate, experimentally and numerically, the effects of Gurney flaps on a NACA 0036. However in the process of this investigation, many problems with the wind tunnel facilities were uncovered. Fighting these fires before accurate data could be recorded amounted to a considerable workload in and of itself. Therefore, the work of restoring the facilities is presented along with the thesis work to enable the committee to gauge the quality and amount of work invested in the project. The additional section provides documentation of the diagnostics performed, the problems found, the actions taken to fix them, and further recommendations to improve the current state of the facilities.

1 Introduction

The motivation of this research stems from the interest in reducing helicopter drag. Fixed-wing aircraft cruise drag is dominated by skin friction drag, which has led to large amounts of research into delaying transition. Helicopter drag differs in that the primary source of cruise drag is attributed to form drag caused by massive separation of the fuselage, rotor hub, nacelles and landing gear. A typical power breakdown is shown in Figure 1. This places tight limits on max performance in range, fuel efficiency and top speed.

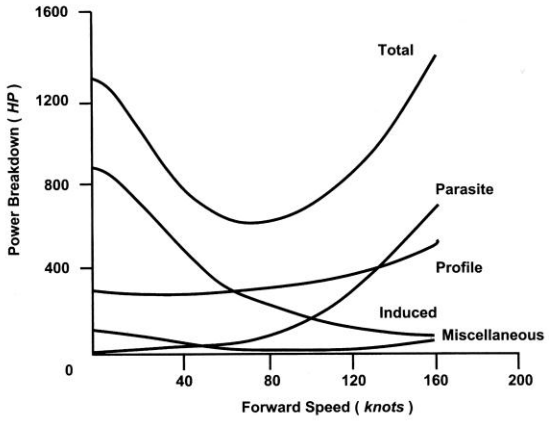

Figure 1 Typical power breakdown for forward flight of a rotorcraft. The reference cites that "parasite" corresponds to fuselage drag, and "profile" corresponds to blade-section drag[1]

As Table 1 suggests, the largest component of drag is the rotor hub. For this study, a NACA 0036 profile is used to simulate the bluff body of a rotor hub or nacelle. This shape does not correspond to a particular geometry but relates more to bluff bodies in general, which also have applications outside of rotorcraft.

Table 1 Typical Breakdown of Parasitic Drag Components on a Helicopter[2]

Component	f/A*	% of Total
Fuselage	0.00210	30
Nacelles	0.00042	6
Rotor hub & shaft	0.00245	35
Tail rotor hub	0.00028	4
Main landing gear	0.00043	6
Tail landing gear	0.00028	4
Horizontal tail	0.00007	1
Vertical tail	0.00007	1
Rotor/fuselage interference	0.00047	7
Exhaust System	0.00021	3
Miscellaneous	0.00021	3
Total	0.007	100

***f/A is the ratio of parasite area to rotor area**

Previous research begins with Martin, Tung and Arad[3] (2003) in studying the effectiveness of synthetic jets on controlling separation. These authors observed a lift-reversal phenomenon, which is characteristic of bluff bodes with sharp trailing edges. Further investigations by the same authors[4] (2006) investigated the complicated computational fluid dynamics (CFD) modeling of the experiment, requiring detached eddy simulation (DES). Successful modeling was only achievable with an ad-hoc adjustment to the near wall turbulence model. This was aided by a Master's Thesis authored by Wilson[5] (2006) on gathering Reynolds stress information in the flow field. In addition, a Cal Poly Master's thesis[6] investigated the effect of placing trip strips in varying locations on the model.

The scope of the current research is to investigate the idea of attaching a gurney flap to the NACA 0036 model and determining its effect on the lift reversal properties. A Gurney flap is a small tab normal to the surface of the airfoil attached at the trailing edge. Previous research has shown Gurney flaps to ease pressure gradients on upper surfaces of airfoils, allowing for delayed separation. The goals of this study are to reduce the

massive separation on the upper surface and to mitigate the lift reversal. Another goal of this study is to further investigate the ability of different CFD modeling techniques to capture the complicated flow characteristics of this body.

2 Background

2.1 Non-linear Nature of a NACA 0036

The NACA 0036 cannot simply be treated as a regular thin airfoil. Typical thin airfoils have linear lift-curve slopes near zero degrees angle of attack which proceed to nonlinear as separation occurs. Because of its large thickness to chord ratio, a NACA 0036 flow field has separation even at zero degrees. As the angle of attack is increased, the separation grows on the upper side, and is eliminated on the lower side. The larger separation on the upper surface mitigates the pressure recovery and lowers the acceleration of the flow, while the bottom surface experiences relatively higher acceleration, creating negative lift. After further increases in angle of attack, the upper surface flow accelerates to produce more suction on the upper surface and positive lift is restored.

For a visual explanation, see Figure 2. This phenomenon was first observed by Horner for airfoils with very sharp trailing edges[7]. In his observation, this occurred at Reynolds numbers of 2.6×10^6. However, he noted that for Reynolds numbers under 1×10^6, lift reversal did not occur.

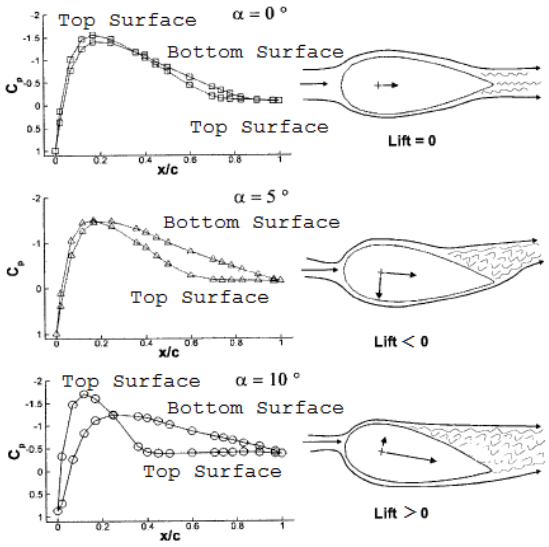

Figure 2 Illustration of lift reversal[8]

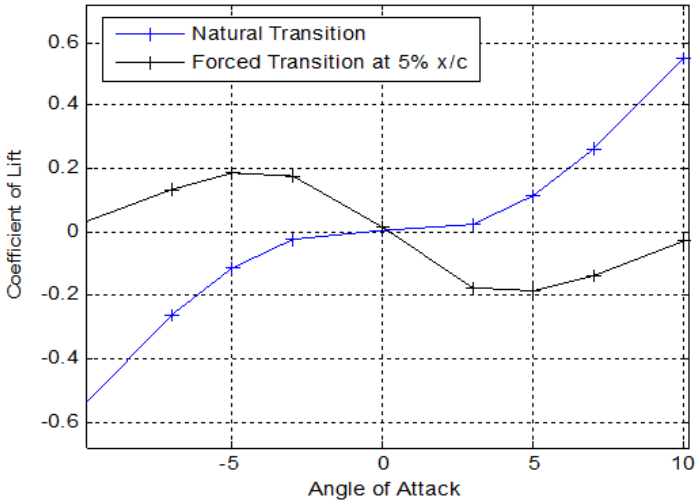

Figure 3 Non-linear nature of a NACA 0036 lift-curve slope (Re ~1e6)

2.2 Boundary Layer Transition

Boundary layer transition refers to the change of a boundary layer from laminar to turbulent flow. Everyday examples of this would be cigarette smoke rising smoothly

then shifting to unsteady random flow, or a garden hose changing from uniformly flowing to sporadic as the pressure is increased. In a flat plate, the onset of transition begins with Tollmien-Schlicting waves, which are 2D oscillations in a viscous boundary layer[9]. In natural transition a laminar separation bubble, or "cat's eye" cross-section, results at the start of these waves[10], as shown in Figure 4. These disturbances can either be damped out or amplified, progressing to 3D, high amplitude disturbances that result in turbulent flow. Transition location is largely dictated by local Reynolds number, but is also very sensitive to pressure gradient, suction or blowing, temperature, free-stream turbulence or pressure/velocity fluctuations and surface roughness[10].

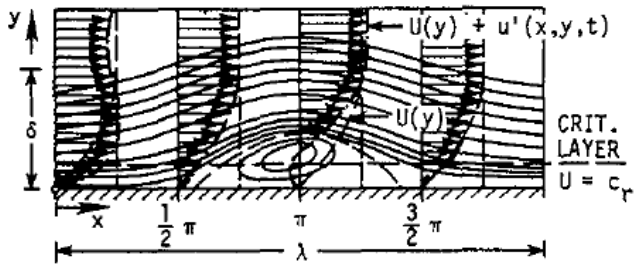

Figure 4 "Cat's eye" disturbance before onset of turbulent flow[10]

Boundary layer transition is very important to aerodynamicists. For high speed transports, early transition would create a higher skin friction drag, which is a large component of drag at cruise conditions. For bluff bodies, early transition would conversely create much lower drag by postponing the separation due to higher energy in the boundary layer, thereby reducing the form drag on the object, i.e. the ripples on a golf ball. Despite its importance, boundary layer transition is still very difficult to predict.

2.3 Transition Strips

Most wind tunnel models use transition strips for two reasons. For one, they make tests more repeatable by fixing the boundary layer transition point in place. They also help to simulate flight Reynolds numbers. For most tests, engineers assume that in higher Reynolds numbers and typical flight conditions transition occurs at the leading edge.

Braslow[11] describes a method to determine the height of the trip strip. He defines a non-dimensional roughness height Reynolds number as

$$Re_k = \frac{u_k k}{\nu_k} \qquad 2\text{-}1$$

where k is the roughness height and $u_k$and ν_k are the velocity and kinematic viscosity at the top of the roughness height, respectively. These terms would be determined by a boundary layer code or flat plate theory. Ideally transition strips are 3D in nature. Previously 2D trips such as wire were used to force transition but studies have shown that 3D trips cause turbulent flow to occur sooner, allowing better control[11].

The trip location is typically found at 5% of airfoils and 10% of bluff bodies[12]. If the strip is placed too far forward the boundary layer can relaminarize. At these percentages the trip is normally aft of the favorable pressure gradient, decreasing the likelihood that the boundary layer will shift back to laminar.

2.4 Separation

Separation is a viscous flow phenomenon in which the boundary layer, under near-wall friction and adverse pressure gradients, detaches from the surface and creates backflow. This can lead to a profile producing large amounts of form drag. At the location of

separation, shear stress is zero because there is zero gradient in u-velocity at the point on the wall, $\tau = \mu \frac{du}{dy} = 0$. Predicting separation in two-dimensional laminar boundary layers with current boundary layer theory is very accurate; turbulent boundary layers, however, are much more complicated.

Cebeci, Mosinskis and Smith[13] review four techniques for predicting two-dimensional boundary layer separation, three of which prove to be in good agreement with experimental data. Examining these techniques is an informative way of seeing what heavily influences turbulent separation. One method covered, Head's Method, uses three empirical relations to solve the momentum integral equation,

$$\frac{d\theta}{dx} + (H+2)\left(\frac{\theta}{u_e}\right)\left(\frac{du_e}{dx}\right) = \frac{C_f}{2} \qquad 2\text{-}2$$

where θ is momentum thickness, H is the shape factor which is the displacement thickness over the momentum thickness ($\frac{\delta^*}{\theta}$), u_e is the inviscid external flow velocity, and C_f is friction coefficient. Once all unknowns are solved, the method predicts separation when H reaches a value between 1.8 and 2.4 (This range is of little importance because H is increasing very rapidly at this point.). This reveals the important concept that a high shape factor results in separation. In other words, high displacement thicknesses with low momentum thicknesses are prone to separation. This is a good quantitative way to foresee the separation.

2.5 Gurney Flaps

A Gurney flap is a short tab at the trailing edge of an airfoil protruding perpendicular to the surface. It was first used by Dan Gurney on his Indianapolis 500 race car to increase aerodynamic down force, which provided a boost in cornering and braking performance. In his field tests, he observed that this flap increased down force, while slightly decreasing drag.[14] Gurney flaps have been the focus of many studies on single element and multi-element airfoils. Common sizes of gurney flaps range from 0.5% to 5% of chord, with most sources citing 2% as an ideal size.

Gurney flaps work by separating flow near the trailing edge, inducing vortices that work to turn the flow. In doing so, pressure is decreased on the suction side and increased on the pressure side. This results in an increase in C_{lmax} of the airfoil and a shift in the zero-lift angle of attack. Gains of 30% of C_{lmax} have been observed for single element airfoils.[15]

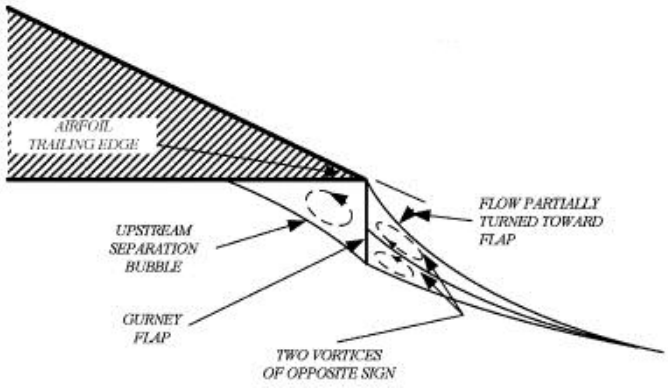

Figure 5 Diagram of vortices created by a Gurney flap[16]

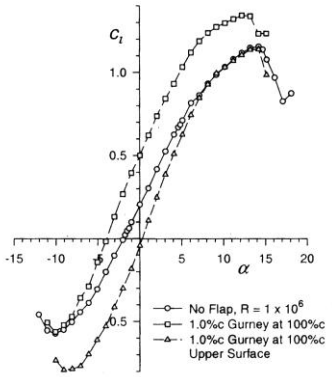

Figure 6 Change in lift-curve from a gurney flap on either side of a S903 natural laminar flow airfoil.[13]

The effect on drag that a Gurney flap exerts is largely dependent on the size of the flap[12,17]. A Gurney flap of 5% can actually increase the lift to drag ratio, while increasing the size has a progressively higher drag penalty. Observations from several researchers have concluded that optimal height for a Gurney flap should be smaller than the boundary layer thickness on the pressure side of the airfoil[12, 15].

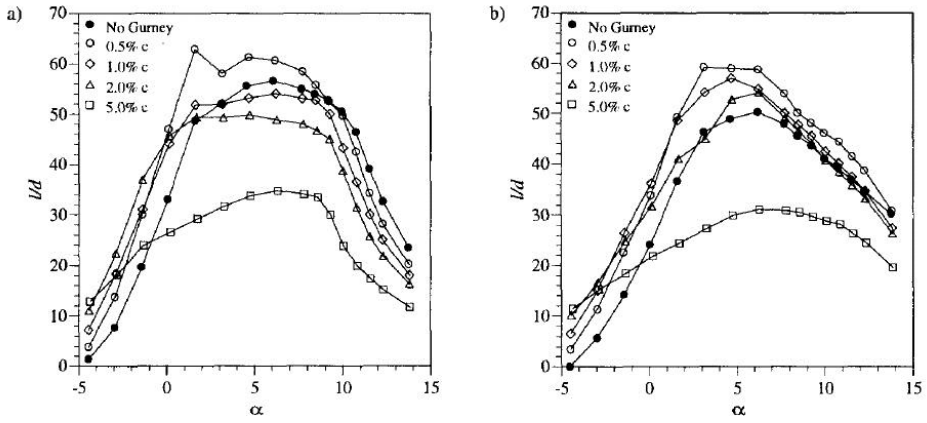

Figure 7 Effect of L/D from a gurney flap on two different airfoils, a) LA203A-UL and b) Gö 797-UL[15]

Giguére[15] also points out that a Gurney flap is most effective at reducing drag when there exists a small amount of trailing edge separation. This observation is the prime motivation of the use of gurney flaps in this study.

3 Experimental Apparatus

3.1 Wind Tunnel Facility

The experiment was conducted in the Cal Poly 3'x4' wind tunnel (precisely 34 ¼"x 46 3/8"). The tunnel is an open-circuit, in-draft design powered by a 150hp, 440 Volt three-phase motor turning a nine-blade suction fan. The inlet to the test section has an 11:1 contraction ratio with newly installed honeycomb and screens for flow straightening. The honeycomb is 1" thick with .15" cell size, followed by three progressively smaller screens, the last of which has a 0.0075" wire diameter and a 0.031" opening. The turbulence intensity for the current configuration is not yet known; however, from recent measurements, the mean stream-wise velocity is estimated to vary less than 1%. Two pressure rings, one behind the last screen and one at the end of the inlet, calibrated by a Pitot-static measurement, are used to set velocity and dynamic pressure. The section configuration started with the inlet, followed by the first test section without the access door, followed by the NASA steel and plexiglass section, which attached to the sting balance section and diffuser. Calibration dynamic pressure was taken on the upstream side of the NASA section without the presence of the model.

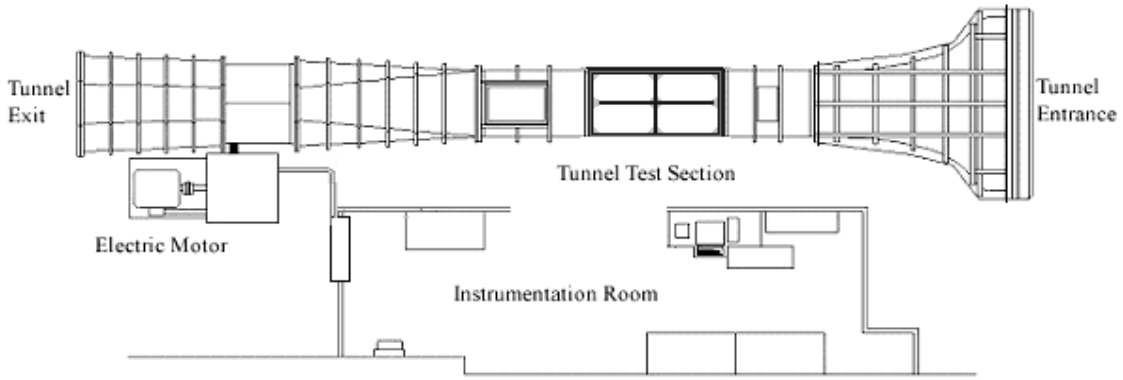

Figure 8 Diagram of wind tunnel configuration[6]

An in-depth study was carried out before the test to determine the state of the wind tunnel. Through many experiments, it was determined that the flow quality was unacceptable and the wind tunnel needed to be repaired. The problem was determined to be poor flow conditioning through the flow straighteners. After the screens and honeycomb were replaced, the tunnel flow was tested and deemed to be acceptable. Details of this study can be found in section 8.

3.2 NACA 0036 Model

The airfoil model used for this study was constructed for a previous experiment[3]. It is a 2D NACA 0036 section with a two foot chord and a finite trailing edge thickness of 0.200". It has 34 pressure ports along its centerline: one at the front center, one on the finite trailing edge, and 16 on each side. These points were located based on flow visualization for angles of attack ranging from 0° to 10°. Both sides have two removable panels installed for synthetic jets. The screw holes to access these panels were filled with museum wax. The model was designed for a 3'x4' cross-section wind tunnel. Despite the large blockage effects seen with the model (the walls are one chord length away and

section blockage ranges between 18-19%), the large chord was chosen for higher Reynolds number scaling. The pivot point is located at 0.433c.

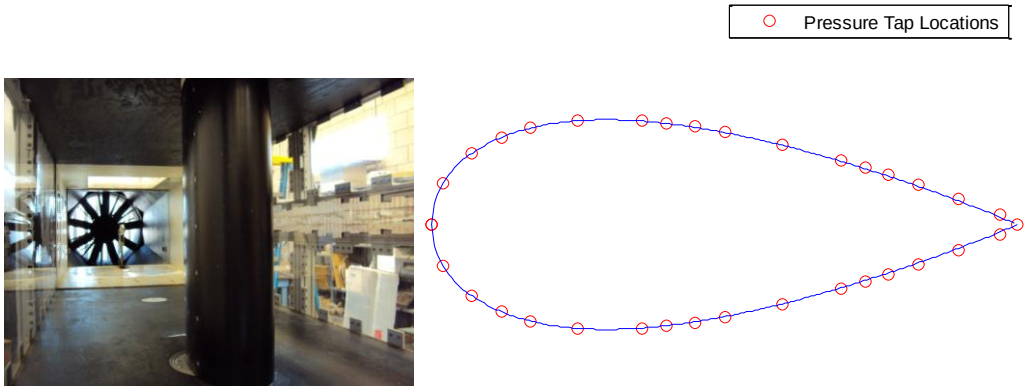

Figure 9 NACA 0036 airfoil photo and tap locations

Some experiments showed slight disagreement with angle of attack. The method used to set angle of attack was originally to mark lines on a piece of paper on the wind tunnel floor and to align the trailing edge to the desired setting. Also, no means existed to change angle of attack without shutting off the tunnel and crawling inside. So for this experiment, turn tables with ball bearings were installed along with and angle of attack indicator to set precisely the angle down to the nearest half degree. A collar was CNC manufactured to ensure a fixed pivot point. Clamps were also required to withstand the large induced moment.

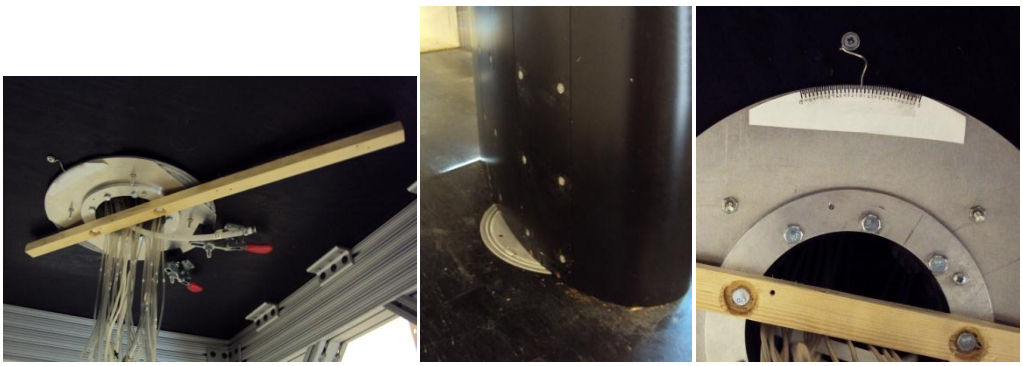

Figure 10 Photos of installed pivot and angle of attack indicator

There were also irregularities seen in the pressure data during the experiment. Completely identical pressure distributions could not be produced without trip strips. This is likely a cause of the slight deformations in the model surface since its creation. As a result, at a geometric zero degrees angle of attack, the lift is non-zero. Figure 11 details this problem. As a result, zero degrees alpha was set with trip strips applied which damped out the slight separation seen below.

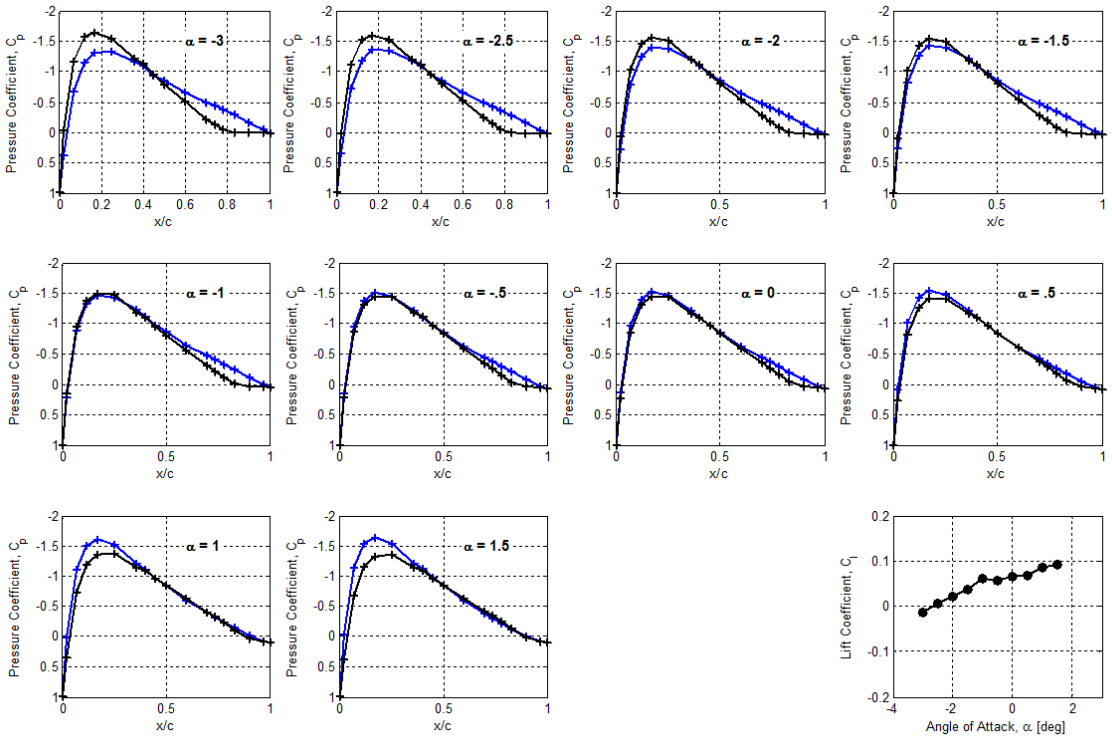

Figure 11 Non-symmetric pressure distribution of the NACA 0036 model with no strips

3.3 Transition Strips

To compare with previous studies, all Gurney flaps and angles of attack were taken with trip strips at 0.05c on both sides of the airfoil in addition to natural transition. This location was determined by earlier studies[3]. Previous experiments used a fine 3M Safety-

Walk™ roughness tape (transparent in color) to force transition. For this experiment, Mini-Logo™ skateboard grip tape was used with pinked (jagged) edges. The theoretically determined roughness heights were significantly smaller than the 3M tape used before. At 5% chord, CFD studies showed the boundary layer height to range from 0.017"-0.020" and U values of 30-40m/s at various angles of attack. With the 0.020" roughness height of the grip tape, R_k values ranged from 970-1143 when only >600 is required to force transition. This supports the flow visualization studies that show successful transition to turbulent boundary layer. Because no smaller transition strip was available, and the pinked grip tape was narrower, thinner and the most 3D to ensure precise transition location, the Mini-Logo™ tape was used. The center of the tape was aligned at 0.05c.

To determine the influence of trip strips on pressure distributions, a small study was performed on three different types of trip strips. A thick 3M Safety-Walk™ (black , 0.029"), thin 3M Safety-Walk™ (clear, 0.022") and pinked Mini-Logo™ grip tape (0.020") were tested. The study showed that no significant differences were observed for any of the strips. Perhaps the larger tape's influence would have been seen in a force or wake measurement because of its protrusion outside of the boundary layer; however, for this experiment, all strips were deemed acceptable.

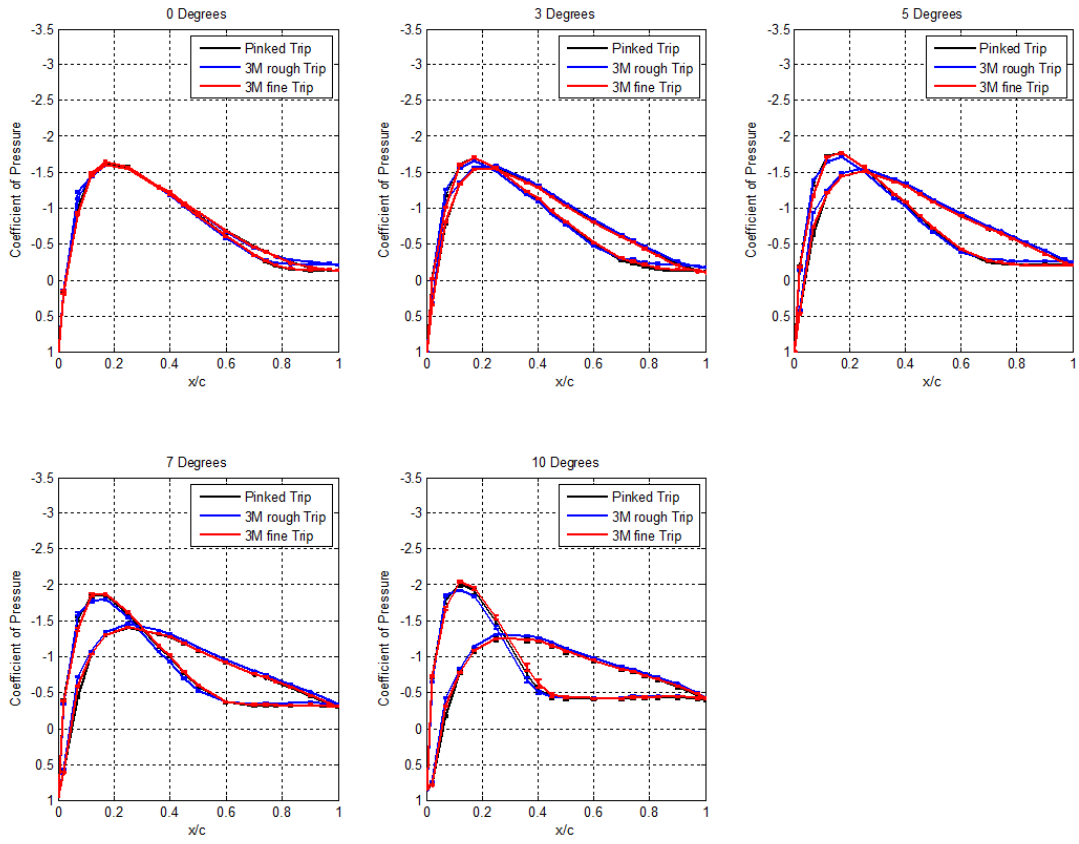

Figure 12 Pressure distributions with three trip strips (thickness: Pinked – 0.020", 3M rough – 0.029", 3M fine – 0.022")

3.4 Gurney Flaps

Five Gurney flaps were constructed, designed to be 1,2,3,4 and 5% of the chord. They were constructed of sheet metal 0.040" thick with an L-shaped cross-section. Each was roughly cut, then milled to precision. They were attached to the airfoil with double-sided tape, as shown in Figure 13. Because of the long flange shape of the Gurney flap, very high precision could not be achieved. However, variances in the double-sided tape thickness made absolute precision difficult to achieve, regardless. Table 2 outlines actual heights of Gurney flaps. These heights were deemed acceptable because only a survey of the design space was desired. *Note: If Gurney flaps were to be used in future experiments, this author would recommend attaching the gurney flaps with small, tapped*

screws. This would allow faster change out, and more precision. The small holes from the installation could be filled in with museum wax, just as the many other holes already are.

Table 2 Manufactured gurney flap heights

Nominal Size (% Chord)	Actual Size (% Chord)	h	b
1%	0.98%	0.236”	0.067”
2%	2.08%	0.499”	0.080”
3%	2.89%	0.693”	0.080”
4%	4.04%	0.970”	0.075”
5%	4.93%	1.182”	0.070”

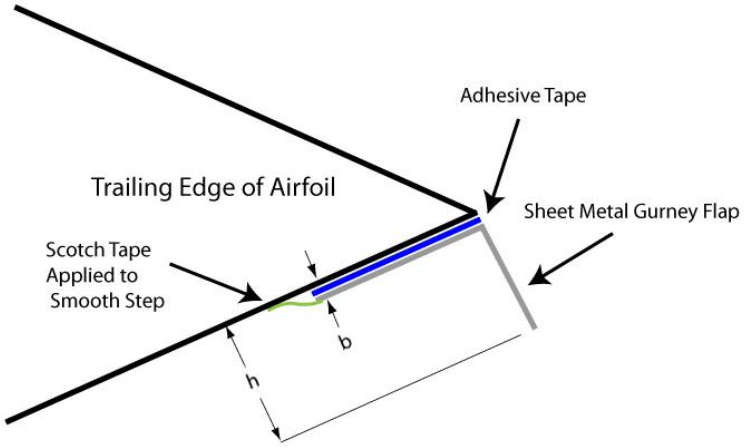

Figure 13 Diagram of Gurney flap installation

3.5 Pressure Measurement

Pressure measurement for this experiment was conducted with a Scanivalve system. The pressure tubes from the model connect directly to the ZOC33/64Px pressure scanner. This unit has 64 differential pressure sensors; the first 32 ports have a ±10 in H_2O

(0.36127 psi) range with accuracy of ±0.15% full scale reading, and the second 32 have a ±1 psi range with accuracy of ±0.10% full scale reading. Temperature sensitivities are 0.25% and 0.10% of full scale reading per °C, respectively. However, the unit is also equipped with an on-board thermal sensor to make temperature drift related adjustments. The designed temperature range for this unit is 0-60°C. The internal multiplexer can scan ports at a rate up to 50kHz. To set zero values, before testing all ports are calibrated to the 'dual range manifold', which for this experiment was always set to ambient pressure. This unit is also capable of conducting a purge of all the lines, which clear the lines of any moisture or debris. The pressure for this feature is provided by 65psi of compressed air attached to the 'calibration control manifold' (This feature was not used in this experiment.).

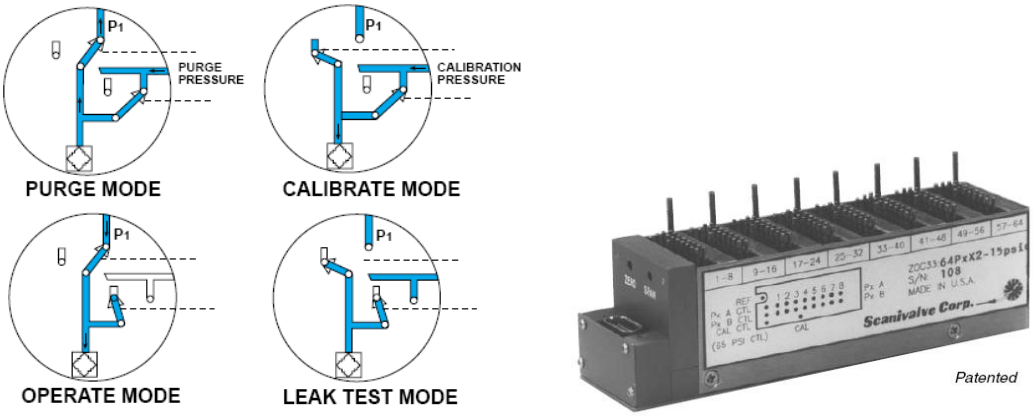

Figure 14 Scanivalve ZOC33-64/Px pressure scanning unit, and associated mode diagram.

The ZOC33 pressure scanning module is connected to the RADBASE3200. This is, essentially, a mini computer that processes signals from up to eight ZOC units. This is where commands are issued to the pressure scanners, temperature adjustments are applied, and units are converted. The RADBASE3200 is designed to communicate using

TCP/IP Ethernet connection. This unit is configured to communicate with a computer via a USB extender unit. The RPM1000 supplies power to the unit.

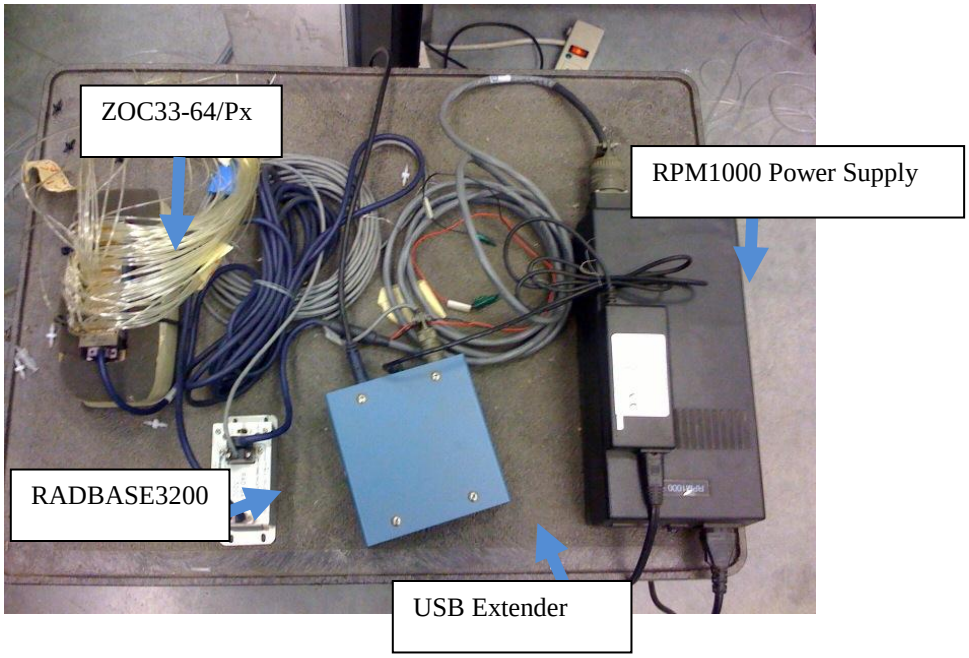

Figure 15 Scanivalve system

4 Experimental Procedure

4.1 Velocity and Dynamic Pressure Calibration

Data was taken with a wind speed of 25 m/s, corresponding to a Reynolds number of $9.96x10^5$ with a 2 ft chord. Velocity was set with pressure rings on the inlet section of the wind tunnel calibrated to a Pitot-static tube at the location of the model in the test section, without the presence of the model. *Note: The Cal Poly wind tunnel is very prone to static pressure losses downstream of the inlet. It is vital that this calibration is performed in an empty test section at the location of the model. Variances of 5% in dynamic pressure were seen over a distance of approximately six feet.* For this calibration, the wind tunnel was set to have the pressure rings to read a difference in pressure of 1.51 inch H_2O. Total and static pressure were read on the scanivalve from the Pitot-static tube as well as the pressure rings behind the screens and throat of the inlet. Calibration constants were determined to be

$$C_q * q_{tunnel} = q_{pitot} \quad (4\text{-}1)$$

$$C_q = 1.0599 \quad (4\text{-}2)$$

$$C_{p_\infty} * p_{\infty_{tunnel}} = p_{\infty_{pitot}} \quad (4\text{-}3)$$

$$C_{p_\infty} = 1.0641 \quad (4\text{-}4)$$

Then C_p was determined by

$$C_p = \frac{p_i - p_{\infty_{tunnel}} * C_{p_\infty}}{\left(p_{T_{tunnel}} - p_{\infty_{tunnel}}\right) * C_q} \quad 4\text{-}5$$

where p_i is a measured surface pressure, $p_{\infty_{tunnel}}$ is the measured pressure at the throat of the inlet. $p_{T_{tunnel}}$ is the pressure measured just behind the screens. After these coefficients were determined, the Pitot-static tube was removed and the model put back in place. Part of this procedure is described in *Low-Speed Wind Tunnel Testing*[12], pgs 218-22.

4.2 Angle of Attack Calibration

Because of the symmetric profile of the model, zero angle of attack was calibrated by aligning the airfoil to a point where both pressures curves were aligned as closely as possible. This calibration was performed on an airfoil with trip strips because surface irregularities had less of an impact.

4.3 Data Collection

Pressure measurements were conducted for airfoil at 0,3,5,7 and 10 degrees. Gurney flaps of 1%, 2%, 3%, 4% and 5% of chord were then installed and measured at all angles of attack. All data was repeated with trip strips at 0.05c. Data was measured using the scanivalve at a rate of 200Hz with 4,000 samples taken. This number was determined to be sufficient for time- averaged data. Note: *This author would recommend faster sampling rates for future tests. Also, the scanivalve must be set to one scan per frame. Otherwise, fluxuation information will be lost.*

4.4 Observable Error Analysis

The measurement uncertainty in C_p must be determined to know the reliability of each data set. The equation of C_p is as follows:

$$C_p = \frac{p_i - p_s * C_{p_s}}{(p_t - p_s) * C_q} \quad \text{4-6}$$

where p_i is the measured pressure, p_t is the total pressure, p_s is the static pressure, and C_{p_s} and C_q are calibrated tunnel constants. In order to determine how the error propagates through this equation, one can say, in general, for some $q(x, y, \dots, z)$ with uncertainties of $\delta_x, \delta_y, \dots, \delta_z$ the uncertainty can be stated as

$$\delta q = \frac{\partial q}{\partial x}\delta_x + \frac{\partial q}{\partial y}\delta_y + \cdots + \frac{\partial q}{\partial z}\delta_z \quad \text{4-7}$$

However, this might overstate the error. If each variable's error is random and independent, the probability of all error maximizing at one time is statistically unlikely. A more accurate estimation of the measurement error would be to take the quadratic sum of the errors, shown by the following equation:

$$\delta q = \sqrt{\left(\frac{\partial q}{\partial x}\delta_x\right)^2 + \left(\frac{\partial q}{\partial y}\delta_y\right)^2 + \cdots + \left(\frac{\partial q}{\partial z}\delta_z\right)^2} \quad \text{4-8}$$

For more information on this technique, refer to *An Introduction to Error Analysis*[18]. Simplifying the partial derivatives, the equation for uncertainty in the coefficient of pressure measurement becomes:

$$\delta C_p = \sqrt{\left[\left(\frac{1}{(p_t - p_s)*C_q}\right)\sigma_{p_i}\right]^2 + \left[\left(-\frac{C_{p_s}}{C_q*(p_t-p_s)} + \frac{p_i - p_s*C_{p_s}}{C_q*(p_t-p_s)^2}\right)\sigma_{p_s}\right]^2 + \left[\left(\frac{p_i - p_s*C_{p_s}}{C_q*(p_t-p_s)^2}\right)\sigma_{p_t}\right]^2} \quad 4\text{-}9$$

where σ is the standard deviation. Using equation 4-4, the reasonable experimental uncertainty can be determined. However, due to long tubing lines to the scanivalve, oscillations in the pressure can be quite low. This element in the system would underestimate the uncertainty related to pressure fluctuations.

4.5 Force Calculation

A standard panel method for determining normal and axial coefficients can be calculated as follows:

$$C_n = \sum_{i=1}^{n} -\frac{1}{2}\Big(C_p(i) + C_p(i+1)\Big)\,(x(i) - x(i+1)) \quad 4\text{-}10$$

$$C_a = \sum_{i=1}^{n} \frac{1}{2}\Big(C_p(i) + C_p(i+1)\Big)\,(y(i) - y(i+1)) \quad 4\text{-}11$$

where $x(i)$ and $y(i)$ are the 2D point locations of the pressure taps. It was found, however, that this method can be improved to more accurately suit the experimental model. Instead of modeling panels between pressure ports, each pressure port was assumed to be a center of one panel. The angle of the panel was analytically determined from the equations that define a NACA 4-series airfoil. The endpoints and corresponding

lengths of each panel can then be determined from this geometry. For the trailing edge point, endpoints were fixed to the width of the measured finite trailing edge of the model. This method assumed to be superior to the first method differed in lift by 5% and in drag by up to 15%. Therefore, the complexity of this method was justified. An image generated by the MATLAB code to run this calculation is shown in Figure 16. Code for this method can be found in Appendix F.

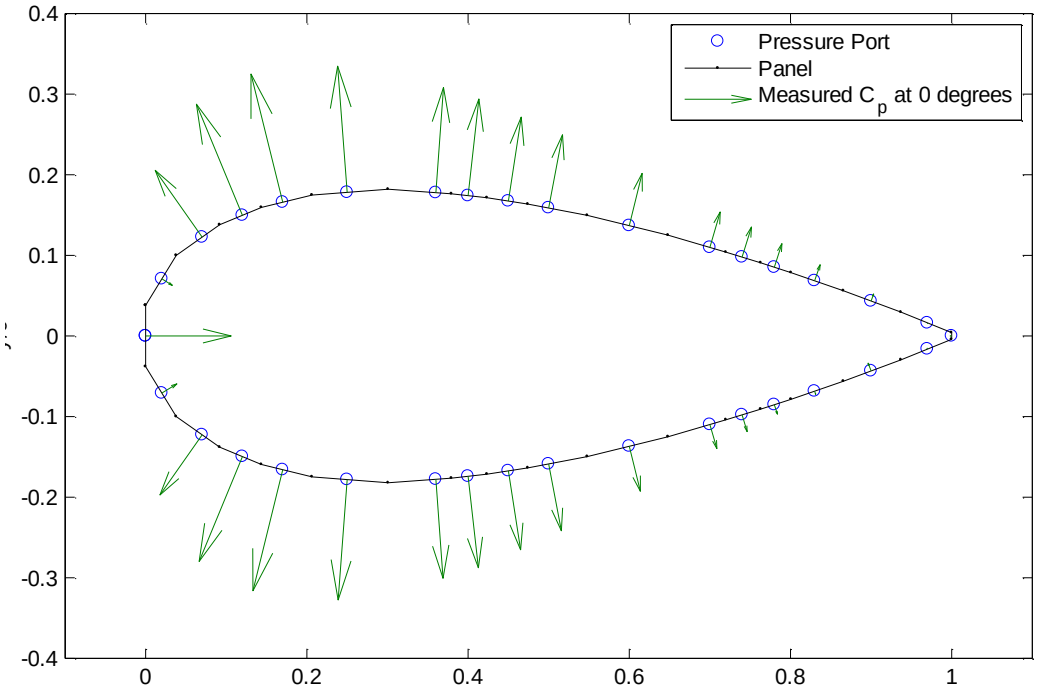

Figure 16 Diagram of panel method used with pressures of a zero degree lift distribution overlaid

After normal and axial coefficients were calculated, they were converted to lift and drag coefficients by:

$$C_l = C_n \cos(\alpha) - C_a \sin(\alpha) \qquad 4\text{-}12$$

$$C_d = C_a \cos(\alpha) + C_n \sin(\alpha) \qquad 4\text{-}13$$

5 Numeric Simulation

5.1 Governing Equations

Computational fluid dynamics (CFD) is generally understood to be any numerical method used to solve a set of equations to model the flow-field of study. For this case, FLUENT was used to solve the Reynolds-averaged Navier-Stokes equations (RANS). These equations are based on the fundamental concepts in physics of conservation of mass, momentum and energy.

5.1.1 Continuity

The continuity equation ensures that no mass is created or destroyed in the system, and that the mass in equals the mass out in steady flow. For an inertial reference frame, the equation can be expressed as:

$$\frac{\partial \rho}{\partial t} + \nabla \cdot (\rho \vec{u}) = 0 \qquad 5\text{-}1$$

where the first term represents the time rate of change of the mass in a control volume element, and the second term represents the time rate of change in mass due to convection.

5.1.2 Momentum Equation (Navier-Stokes Equations)

The next set of equations establishes a conservation of momentum in each spatial dimension. In the current 2D study, only equations for the x and y direction were solved. The equations can be expressed as:

$$\frac{\partial}{\partial t}(\rho\vec{u}) + \nabla \cdot (\rho\vec{u}\vec{u}) = -\nabla p + \nabla \cdot (\bar{\bar{\tau}}) + \rho\vec{g} \qquad 5\text{-}2$$

The first term represents the time rate of change of the momentum into the volume element; the second term represents the change in momentum due to convection; the third is the change due to pressure forces; the fourth represents the rate of change due to viscous forces, and the last is the change due to gravitation.

5.1.3 Energy Equation

The energy equation is required whenever heat transfer or pressure work is present in the flow. For the current case, the flow is assumed to be incompressible and constant viscosity (which is related to temperature); therefore the energy equation is not solved. Instead, a pressure based solver is used, which decouples the pressure and velocity terms. For more information, refer to the SIMPLE algorithm[19].

5.1.4 Reynolds Averaging

In order to simplify flow characteristics, the quantities in the Navier-Stokes equations are separated into time-dependent, turbulent fluctuations (denoted as ϕ') and "time-averaged" quantities (denoted as $\bar{\phi}$) that represent the changes that are of interest in the flow quantities. This is analogous to a low-pass filter in which all unsteady quantities that are very high frequency are separated out so that only low frequency fluctuations can be examined. This assumption is valid for steady-state problems as well as some unsteady problems but is not valid for problems such as acoustic modeling where high frequency fluctuations are of interest. Using this assumption, the Navier-Stokes equations can be re-written in Einstein notation as:

$$\rho \frac{\partial \bar{u}_j \bar{u}_i}{\partial x_j} = \rho \bar{g}_i + \frac{\partial}{\partial x_j}\left[-\bar{p}\delta_{ij} + \mu\left(\frac{\partial \bar{u}_i}{\partial x_j} + \frac{\partial \bar{u}_j}{\partial x_i}\right) - \rho\overline{u_i' u_j'}\right] \quad 5\text{-}3$$

The most challenging part of this equation is the last term $-\rho\overline{u_i' u_j'}$, which is called the Reynolds stress tensor. This is the focus of most present day turbulence modeling.

5.2 Turbulence Modeling

5.2.1 The Boussinesq Approximation

In 1877, Joseph Boussinesq proposed that the Reynolds stresses could be modeled by a fictitious "eddy" viscosity. His assumption states that:

$$-\rho\overline{u_i' u_j'} = 2\mu_T S_{ij} - \frac{2}{3}\delta_{ij}\left(\mu_T \frac{\partial \mu_k}{\partial x_k} + \rho\bar{k}\right) \quad 5\text{-}4$$

where μ_T is the turbulent viscosity, $\bar{k}$ is the turbulent kinetic energy, and S_{ij} is determined by:

$$S_{ij} = \frac{1}{2}\left(\frac{\partial \bar{u}_i}{\partial x_j} + \frac{\partial \bar{u}_j}{\partial x_i}\right) \quad 5\text{-}5$$

Introducing the two terms μ_k and $\bar{k}$ requires two additional equations[19]. However, this assumption is the foundation of all eddy viscosity turbulence models.

5.2.2 Turbulence Models

There are numerous turbulence models available; therefore choosing one for a particular problem can be somewhat difficult. Little weight is given to models with strong theoretical backing; there have been far too many assumptions made thus far. Therefore, the success of a turbulence model is primarily determined by its high correlation with experimental data. It is the author's experience that two models have become fairly widespread, the Mentor $k-\omega$ SST model and the $k-\epsilon$ Realizable model. The $k-\epsilon$ Realizable model is a set of two partial differential equations that is used to determine ε and $\bar{k}$. Mentor's $k-\omega$ SST model is more complicated, and blends $k-\omega$ near the walls with $k-\varepsilon$ away from the walls. These two models were employed for the current problem, as well as a model newly provided by FLUENT 12.1 that attempts to model transition. The details of their implementation can be found in the FLUENT documentation.

5.3 Mesh Approach

GAMBIT 2.2.30 was used to create the 2D mesh. Three mesh styles were attempted before the final mesh was selected. The first mesh approach was to have a structured domain and an unstructured interior zone with prism cells to capture the boundary layer. This was unsatisfactory because mesh cells created near the trailing edge were highly skewed. Because they were often located in separation, they would cause slight convergence problems. A completely structured H-grid was also attempted; however, the blunt leading edge of the NACA 0036 airfoil resulted in highly skewed cells that could not be corrected with smoothing algorithms within GAMBIT, especially at high angles of attack.

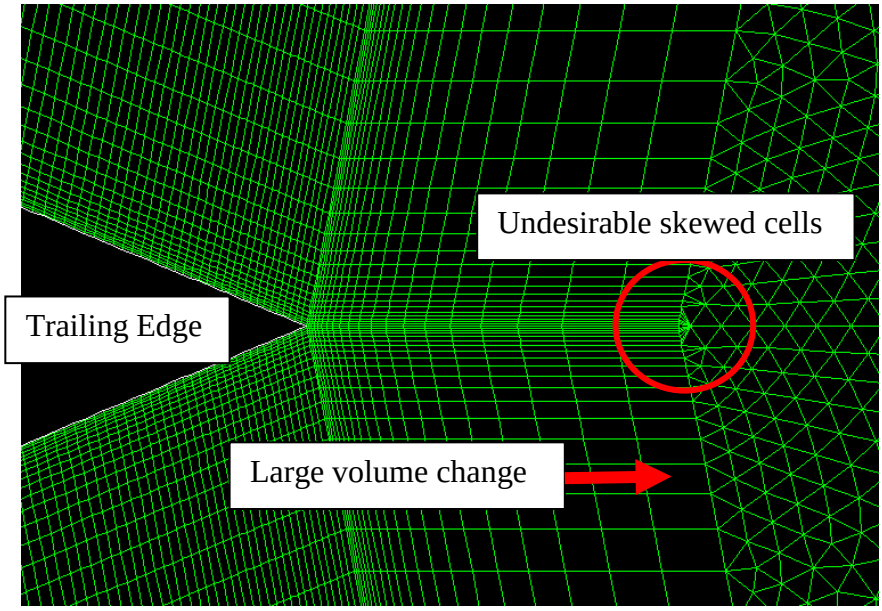

Figure 17 Undesirable qualities of first mesh approach

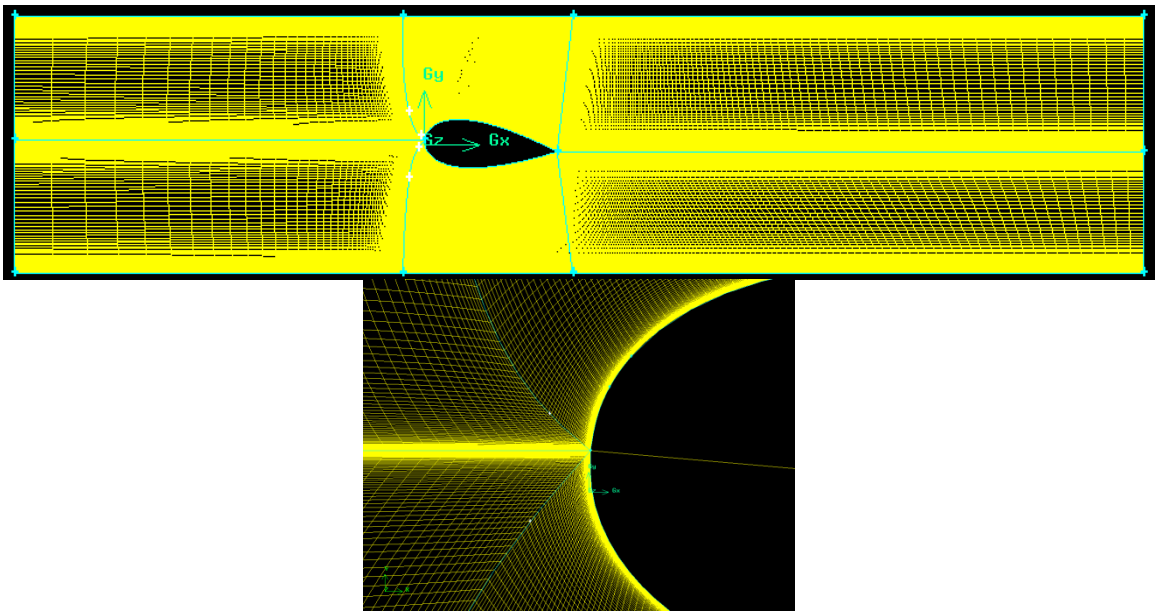

Figure 18 Second mesh approach contained too many skewed cells in front of leading edge, causing diverging solutions

The final mesh approach was somewhat of a hybrid between these two techniques and produced the highest quality mesh. The mesh had a structured mesh in close proximity of the airfoil which extended through the rear domain. Outside of that was an unstructured

zone that transitioned to the structured domain far from the airfoil surface. Figure 19 shows this in detail. All walls including wind tunnel walls were sized to produce y^+ of less than one. This was verified with a converged solution. The domain was sized according to actual wind tunnel dimensions: 46.375" tall, 74" in front of the leading edge, and 130" behind the trailing edge (1.93, 3.08, and 5.42 chord lengths respectively). This resulted in a 68,000 cell mesh.

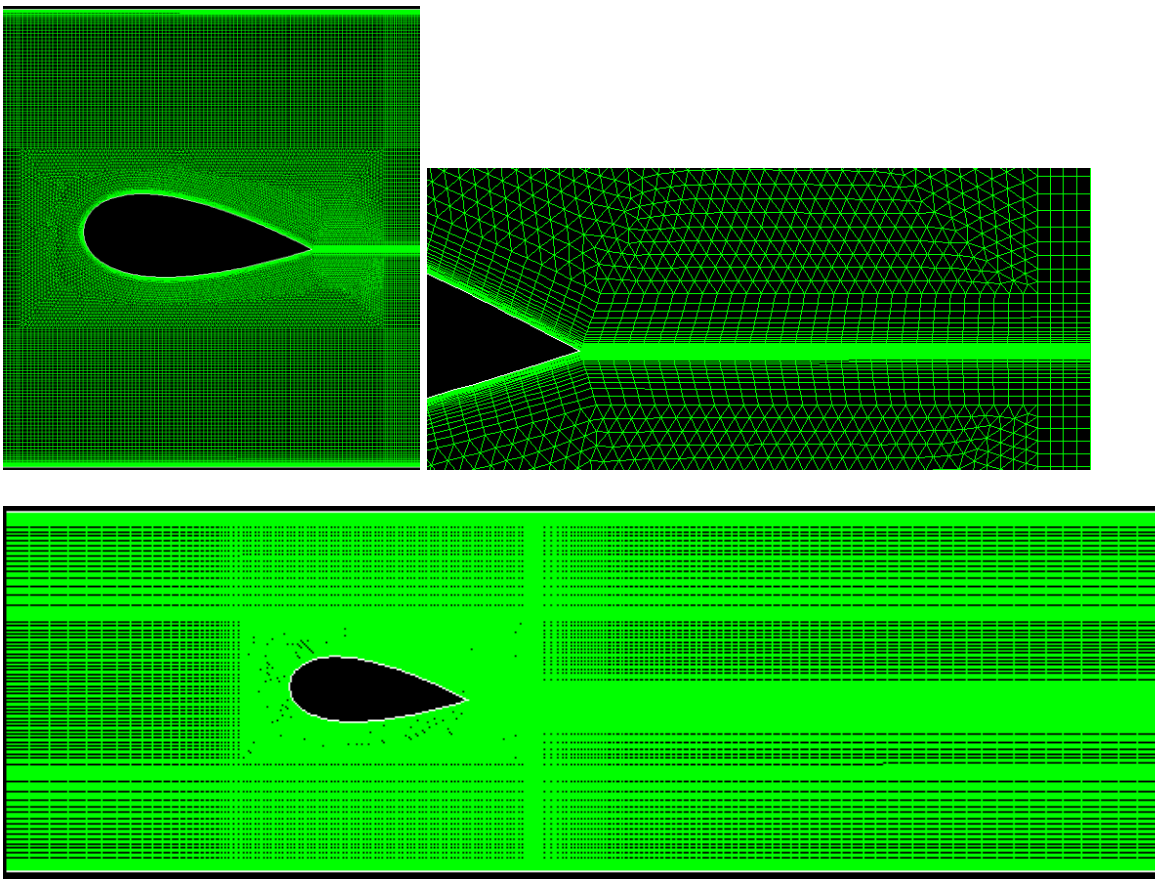

Figure 19 Final mesh approach

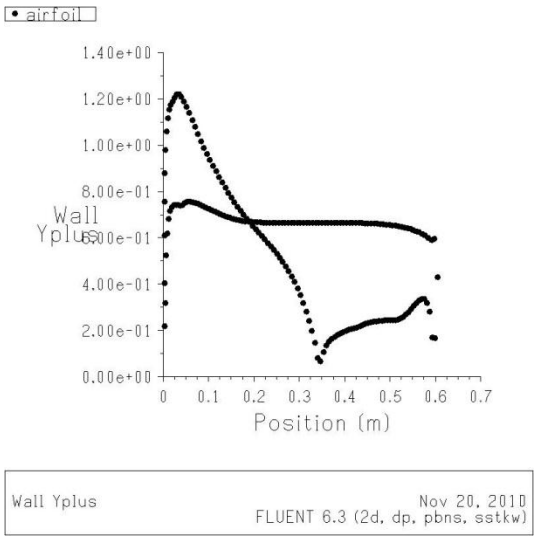

Figure 20 Example of Y^+ values

5.4 Solver Settings

FLUENT 12.1 was used to resolve the RANS equations over the mesh. A 2D, steady-state, pressure based solver was implemented. The Green-Gauss node based gradient option was selected for its preservation of second order accuracy on triangular cells[20]. Mentor's k-ω SST and k-ε Realizable were both used to determine which turbulence model was more successful in modeling the flow of interest. For k-ε Realizable, enhanced wall treatment was employed to give mesh cells with y^+ of 1 proper treatment. Second order upwind discretization was used for all equations solved. The SIMPLE scheme was used to resolve the pressure-velocity coupling.

5.5 Boundary Conditions

Wall boundary conditions (with enhanced wall functions with k-ε) were applied for the wind tunnel walls and the airfoil surface. A 'velocity-inlet' condition was applied for the inlet, with a speed of 25m/s. Outlet was set to 'pressure-outlet'. For inflow turbulence, the intensity and viscosity ratio specification method was specified with a turbulence

intensity of 0.5% and turbulent viscosity ratio (the ratio of eddy viscosity to dynamic viscosity) of 2.

5.6 Convergence Criteria

For convergence criteria, the lift data was monitored for several cases. Once the number of iterations was known to allow the force data to approach a steady rate, 4000 iterations for this study, the CFD cases were simply set to run a fixed number of iterations.

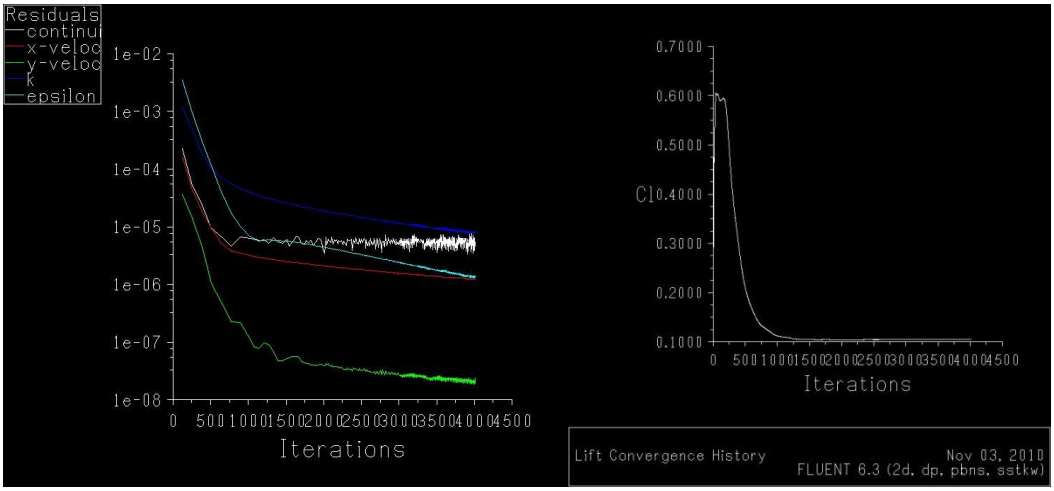

Figure 21 Residuals verses iterations and lift coefficient verses iteration. Drag plot (not shown) similar to lift coefficient

5.7 Data Post-Processing

The post-processing of the CFD data was complicated by the way FLUENT exports the pressure data. FLUENT prints out pressure data with respect to the x-values; however, for a fair comparison to experimental data the pressure data must be plotted with respect to the chord line. All pressure data from CFD was transformed by rotating the points around the center of rotation back to zero degrees. In addition, the reported force data were only the pressure forces without the viscous components.

5.8 Mesh Independence

To determine the sensitivity of the solution on the mesh parameters, a mesh independence study was performed according to the Journal of Fluids Engineering[21]. The method involves five steps to evaluate the error on given parameters. For this study, C_p values at the pressure tap locations on the experimental model were the parameters chosen.

Three different grids of varying density were solved on for the NACA 0036 at 10 degrees, with cell counts of 34,000, 68,000 and 135,000. When cells were added, efforts were made to distribute them evenly across the mesh.

The first step of the method is to calculate a representative cell size, *h*. The area of each mesh was 6.371m^2. The number of cells divided by the area gave the average area per cell, which was 0.0137, 0.00968, and 0.00384 m^2 respectively. The second step is to simply find the ratio between these sizes, which is $r_{21} = 1.41$ and $r_{32} = 1.42$ (1 being the fine grid, and 3 being the coarse grid).

The third step is to solve the set of equations for p:

$$p = \frac{1}{\ln(r_{21})}\left|\ln\left|\frac{\varepsilon_{32}}{\varepsilon_{21}}\right| + q(p)\right| \quad 5\text{-}6$$

$$q(p) = \ln\left(\frac{r_{21}^{p} - s}{r_{32}^{p} - s}\right) \quad 5\text{-}7$$

$$s = 1 \cdot sign\left(\frac{\varepsilon_{32}}{\varepsilon_{21}}\right) \quad 5\text{-}8$$

where $\varepsilon_{32} = \phi_3 - \phi_2$, $\varepsilon_{21} = \phi_2 - \phi_1$, and ϕ_i is a data point from each grid. With a few simplifications, this can be solved with MATLAB's `fzero()` function. Once solved, p gives the apparent order of the method. The Journal does note that if ε_{32} or ε_{21} are "very close" to zero, the method does not work and might suggest oscillatory convergence.

After p is determined for each data point, step four is to calculate the extrapolated solution using the following equation:

$$\phi_{ext}^{21} = \frac{r_{21}^p \phi_1 - \phi_2}{r_{21}^p - 1} \tag{5-9}$$

The last step is to calculate the fine-grid convergence index (GCI) which will be used to bound the solution uncertainty. This can be determined by the following equations:

$$e_a^{21} = \left| \frac{\phi_1 - \phi_2}{\phi_1} \right| \tag{5-10}$$

$$GCI_{fine}^{21} = \frac{11.25 e_a^{21}}{r_{21}^p - 1} \tag{5-11}$$

Once the GCI is determined, it can be used to plot error bounds over the solution.

Figure 22 shows the solutions produced by the three different meshes and the extrapolated solution. Out of the 35 data points measured, 27 of them were oscillatory in convergence which signifies very high mesh sensitivity on the solution. There exists a very large outlying point on the upper surface at the point of separation for the extrapolated result. This is a clear failure of the method, and is a strong sign of oscillatory convergence. The differences of the point were "very close" to zero, which is a stated shortfall of the method. This could be a result of the CFD solution being unable to determine the exact point of separation for a large separation zone. Although less

abrupt, there are also extrapolated values near the trailing edge that deviate from the three solutions. Again, this signifies difficulty of the solution to spatially resolve the separation.

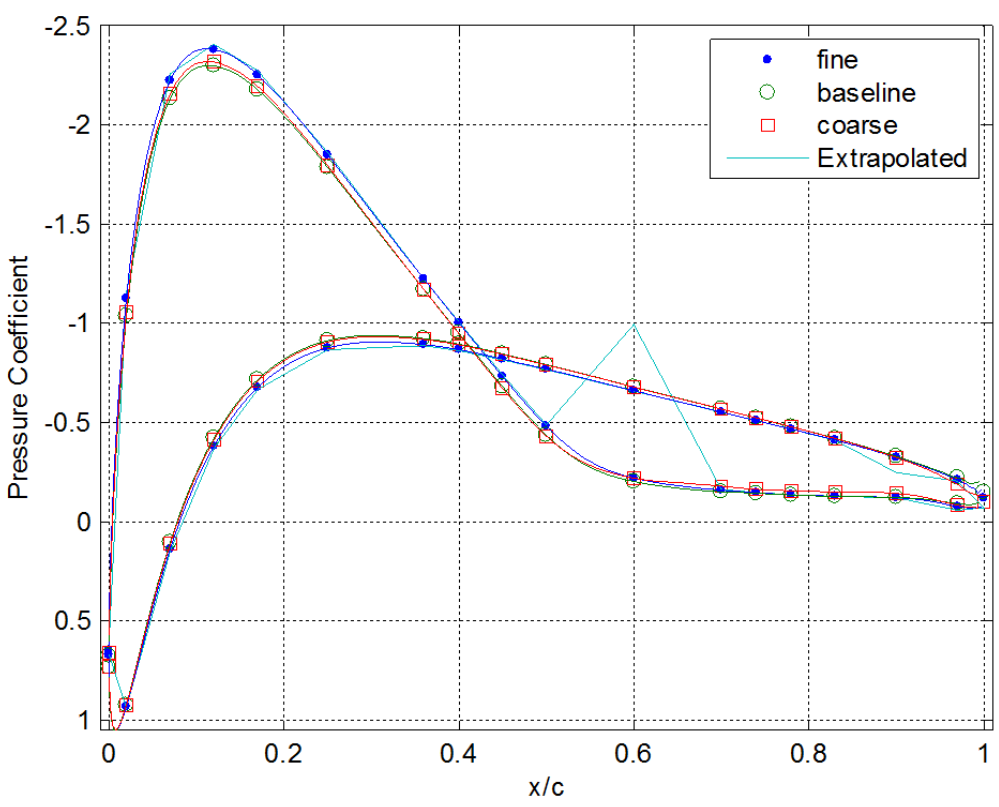

Figure 22 CFD results of a pressure distribution over the NACA 0036 at 10 degrees using three different size meshes, and the extrapolated solution

Below, Figure 23 shows the extrapolated CFD solution with the error bars from the GCI. The one large outlier noted before (0.6 x/c, upper surface) was replaced with the fine grid data point. The error bars represent the uncertainty of the CFD solution as a result of mesh discretization. Notice the high error bars on each of the outliers which were pointed out previously. Data from this graph can be compared to experimental data to gain insight on how well the CFD actually models the flow field.

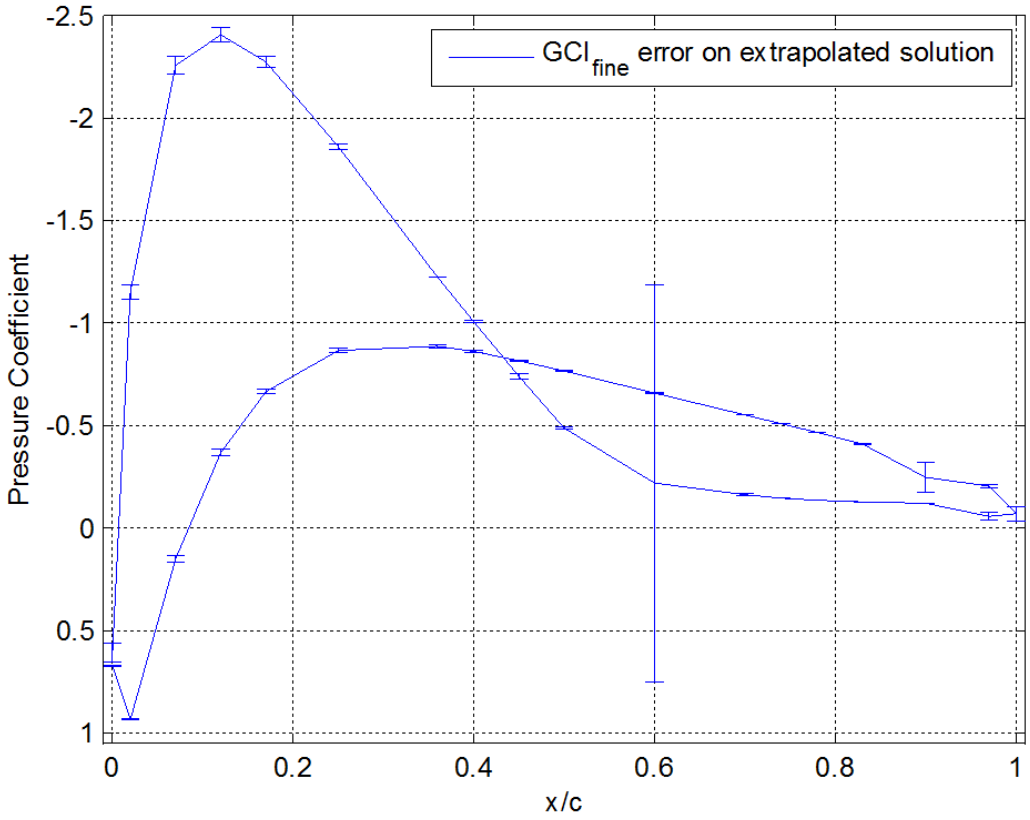

Figure 23 GCI error bars on the extrapolated CFD solution of a NACA 0036 at 10 degrees

6 Results and Discussions

6.1 Wind Tunnel Experiment

Before testing Gurney flaps, the baseline data was compared with previous data in order to verify the accuracy of measurement equipment and procedure. Figure 24 shows the comparison of current data to two sets of previous data for airfoils with trip strips at 0.05c on both sides of the airfoil. At zero angle of attack, the current data shows good agreement of the two symmetric sides of the airfoil. For higher angles of attack, slight variances arise in the point of separation. This might be a result of the sonic choke at the end of the NASA tunnel used in the Martin data, because both Jacob's data and the current experiment were tested in the Cal Poly low speed wind tunnel. A sonic choke prevents interactions from the unsteady wake with the diffuser to propagate upstream. The main difference in the current data is a 5-6% higher peak negative C_p at 5 and 10 degrees angle of attack. This can be attributed to larger boundary layers in the wind tunnel test section resulting from a different tunnel section configuration.

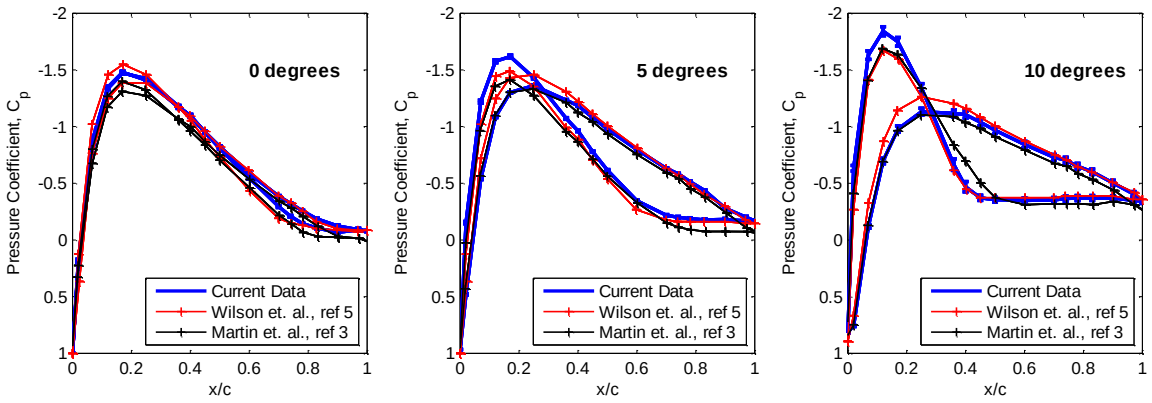

Figure 24 Comparison of baseline data to former experiments: all airfoils are tripped at 0.05c and tested in 4'x3' wind tunnels at Re ~1e6.

All data was also taken with trip strips at 0.05c on both sides of the airfoil and also without trip strips. Figure 25 shows the significant effect of these trip strips.

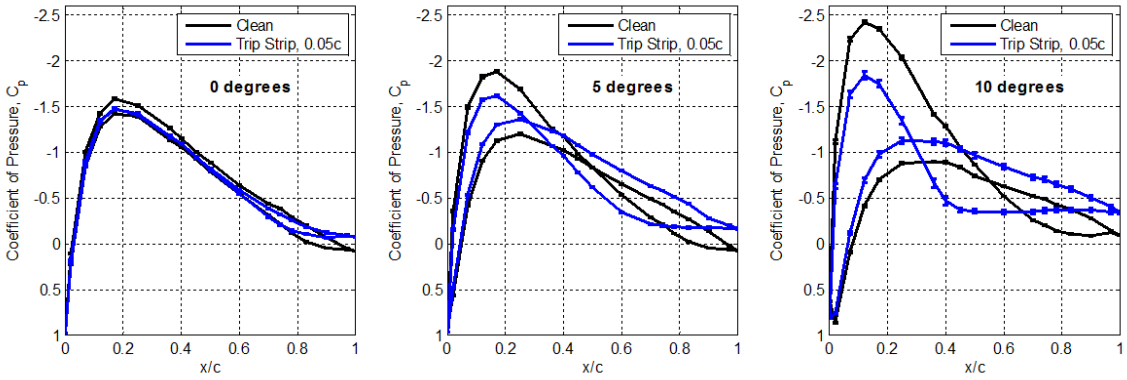

Figure 25 Pressure coefficient of NACA 0036 with and without trip strips

Tripping the boundary layer shows a larger separation, shown by a flattening out of the pressure distribution. To understand this phenomenon, take the example of a cylinder. For a smooth circular cylinder, once the cylinder reaches the critical Reynolds number, transition occurs and the boundary layer has the added momentum of a turbulent boundary layer to remain attached for longer. However, in the present case transition already occurs, just later than 5% of chord. Tripping the boundary layer early causes larger boundary layer growth due to the higher growth rate of turbulent boundary layers. The trip strip also creates an added displacement thickness. Recall Equation 2-2, which states that a boundary layer with a higher displacement thickness and a constant or lower momentum thickness is more likely to separate. In addition, the clean airfoil shows significantly higher negative C_p peaks at both 5 and 10 degrees. This is because larger separated regions reduce pressure peaks, just as the pressure peak of a NACA airfoil drops as it approaches stall.

Figure 26 shows the effect of adding a Gurney flap to a clean (natural transition) airfoil. For clarity only 1, 3, and 5% Gurney flaps are shown. Complete data can be found in Appendix A. At zero angle of attack, only the 5% Gurney shows any deviation over the suction peak. For higher angles of attack, much more deviation is seen over the peak, but the separation point is not changed. At high angles of attack the Gurney flap does not mitigate separation as predicted.

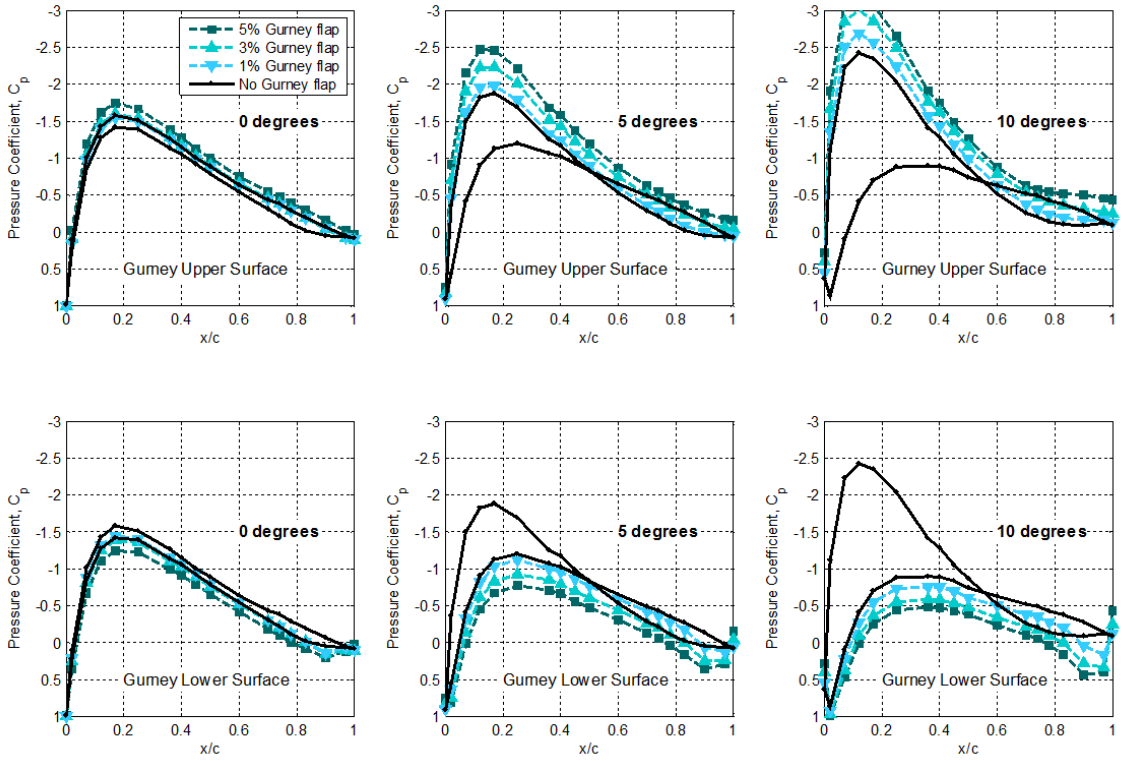

Figure 26 Effect of Gurney flaps on an untripped NACA 0036

The same data was also taken with transition strips at 0.05c and is shown in Figure 27. Again, only 1%, 3%, and 5% Gurney flaps are shown for clarity. Similar trends can be seen with the tripped data when compared to the clean data. One noticeable difference is that the effect of the Gurney flap at zero degrees is much less with a tripped boundary

layer. This is because the boundary layer thickness is larger and decreases the effectiveness of the Gurney flap. This trend also continues at higher angles of attack.

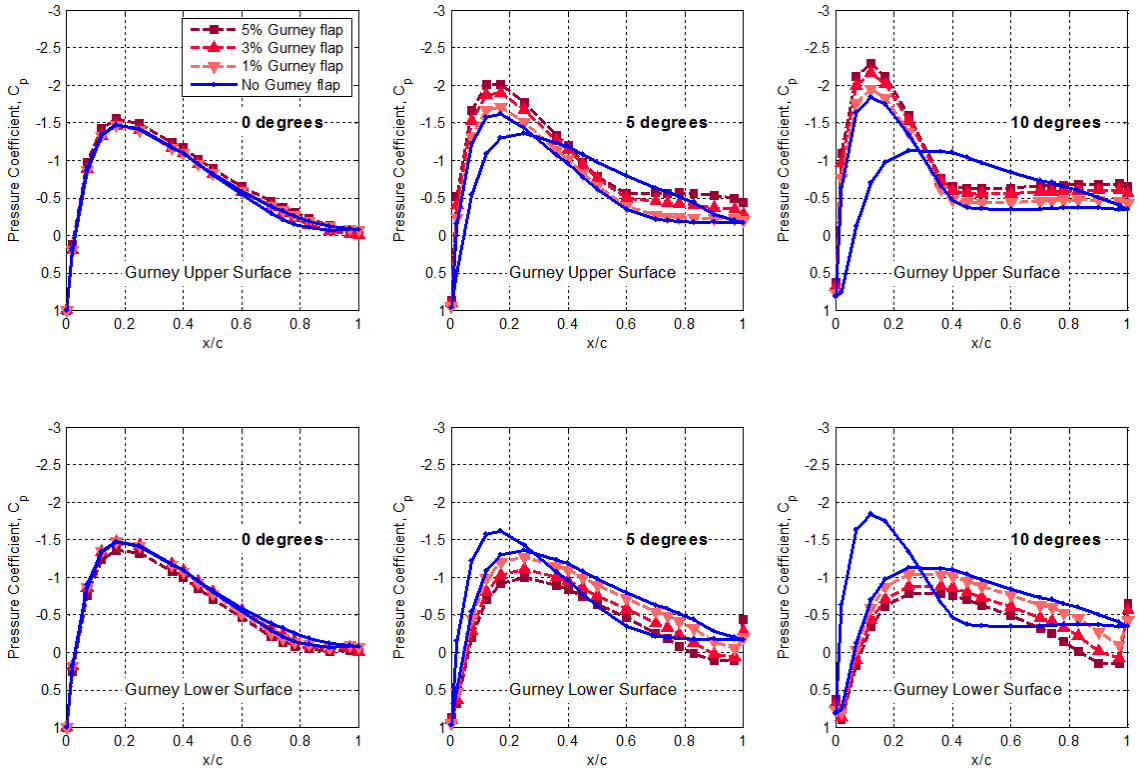

Figure 27 Effect of Gurney flaps on a NACA 0036 with transition strips placed at 0.05c on each side

Despite the asymmetric Gurney flap, there is no effect of the flap at negative angles of attack, even with the largest flap tested. However, because this data was only recorded before fixes to the tunnel were made, it is only included in Appendix A.

Force data was calculated by integrating the pressure over the surface with a panel code. This produces lift and the pressure component of drag, but not viscous drag. Figure 28 shows the force data for a smooth wing with varying Gurney flaps. Lift is non-zero at zero angle of attack because of imperfections of the wing surface (which are surprisingly diminished with a tripped boundary layer, shown later). All Gurney flaps produce less drag at zero angle of attack, but this advantage is quickly lost as angle of attack is

increased. However, this does not include the drag on the flap, which would require force data to accurately measure. The lift curve slope is also straightened out to produce a linear lift curve slope typical of a normal thin airfoil, with higher lift for lager Gurney flap. The lift to drag ratio is vastly improved as the Gurney flap size is increased, an effect usually not observed with Gurney flaps. Normally, Gurney flaps decrease the lift to drag ratio after 0.005-0.02c[4]. In drag and L/D, the positive effect of the Gurney flap is rapidly diminished as angle of attack is increased.

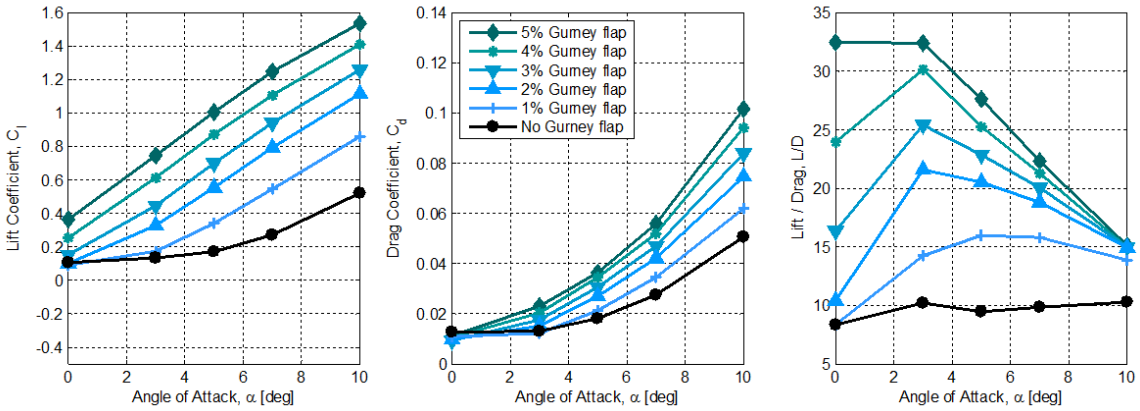

Figure 28 Lift, Drag, and L/D data for Gurney flaps on a clean NACA 0036 (no trip)

The force data for the tripped case is shown in Figure 29. Here, the lift-reversal phenomenon is observable. At zero angle of attack, lift is essentially zero, which is the behavior expected. The lift curve slope does not appear linear with the addition of a Gurney flap, even with a 5% Gurney flap. However, lift reversal is eliminated with 2% and larger Gurney flaps. High non-linearity also arises in drag as the Gurney flap size is increased. This fact was confirmed by several measurements. At zero angle of attack, a drag reduction still remains for the tripped case and appears slightly less sensitive to angle of attack. Lift-to-drag ratios are still improved with increasing flap size, but are much less in magnitude to the non-tripped case.

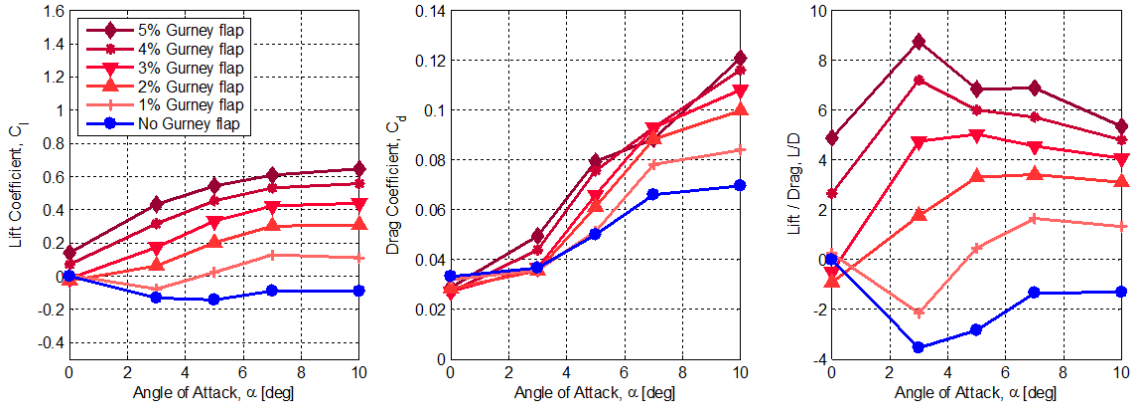

Figure 29 Lift, Drag, and L/D data for Gurney flaps on a NACA 0036, with tripped boundary layer at 0.05c

To quantitatively evaluate the drag benefits from Gurney flaps at low angles of attack, Table 3 is provided. At zero degrees, all Gurney flaps tested show a decrease in drag, with a max reduction of 27% and 18% for non-tripped and tripped airfoil, respectively. With a 2% Gurney flap, the lift reversal is eliminated and the drag of the wing is reduced at low angles of attack. Most drag reductions are eliminated with an increase of just three degrees in angle of attack. Also, a larger Gurney flap is more effective when the boundary layer was tripped; the best size was 0.04c compared to the 0.03c Gurney flap for natural transition.

Table 3 Drag figures for low angles of attack

Angle of Attack: 0 Degrees	**Form Drag, Natural Transition**	**Form Drag, Trip Strip at 0.05c**	**Angle of Attack: 3 Degrees**	**Form Drag, Natural Transition**	**Form Drag, Trip Strip at 0.05c**
Clean Airfoil	0.0128	0.0332	**Clean Airfoil**	0.0123	0.0367
1% Gurney Flap	0.0109 (-15%)	0.0320 (-4%)	**1% Gurney Flap**	0.0112 (-9%)	0.0358 (-2%)
2% Gurney Flap	0.0098 (-23%)	0.0284 (-14%)	**2% Gurney Flap**	0.0152 (+24%)	0.0356 (-3%)
3% Gurney Flap	0.0094 (-27%)	0.0272 (-18%)	**3% Gurney Flap**	0.0176 (+43%)	0.0368 (~0%)
4% Gurney Flap	0.0106 (-17%)	0.0270 (-19%)	**4% Gurney Flap**	0.0204 (+66%)	0.0439 (+20%)
5% Gurney Flap	0.0112 (-13%)	0.0289 (-13%)	**5% Gurney Flap**	0.0230 (+87%)	0.0495 (+35%)

Because the 2% Gurney flap would seem the most desirable for drag and lift benefits, a more refined study was conducted with respect to angle of attack. Figure 30 shows the lift and drag curves with data refined to one degree. Because of the asymmetry of the Gurney flap, negative angles of attack were also measured. Little effect can be seen at these negative angles because at this point the Gurney flap falls in the wake of the airfoil. Data on this plot is slightly different than displayed in the table above. In comparison of the surface pressures, the result is from high sensitivity in the model due to changing of removable plates (they had to be removed and reinstalled between these data sets). This possibly signals the fickle and sensitive nature of this drag savings.

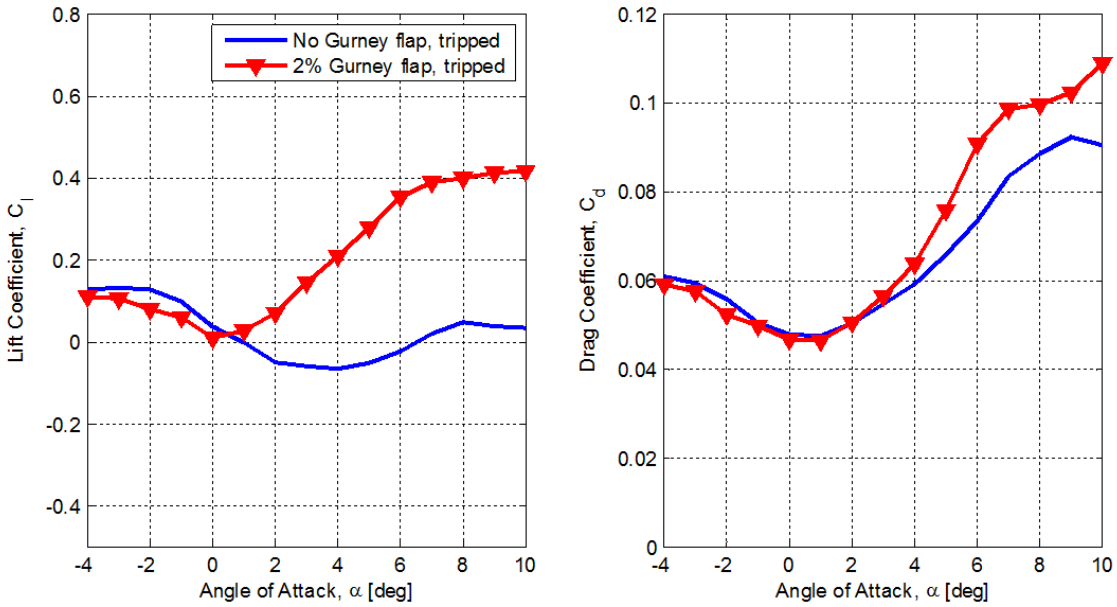

Figure 30 Refined lift and drag data for 2% Gurney Flap

6.2 CFD Simulation

Because of problems with the wind tunnel facility, less time was devoted to the CFD study than initially expected. The current study does not represent a completely adequate correlation with experimental data; however, it serves as a strong base for further analysis if closer correlation is required.

CFD simulations were run using FLUENT 12.1 software to gain better insight into the experiment. This experiment, though only 2D in nature, is difficult to model in CFD because of the large region of separation observed. Also, because the trip strip selected has such a strong effect on the boundary layer, only the clean data was simulated. Therefore, this should serve the reader as a first-cut attempt in modeling the problem in CFD. If more accurate modeling is desired, further assumptions must be dropped and/or higher fidelity techniques must be implemented.

Figure 31 shows the clean experiment data to CFD solutions for three different turbulence models: k-ω SST, k-ε realizable and a k-ω transitional model, new to FLUENT 12.1. Fair correlation is observed with the simulations and clean experiment. However, for k-ω SST (traditionally the most accurate) the point of separation is incorrectly predicted but the pressure side of the airfoil is accurately modeled. The two other turbulence models come closer with the point of separation but do not accurately predict suction peak values and lower surface pressure. All models under-predict the separation on the wing but the k-ε and the transition model come much closer.

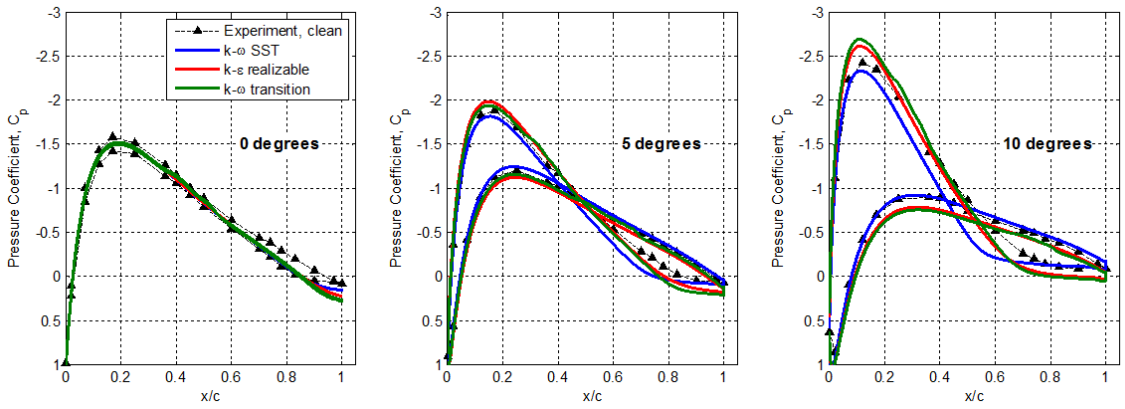

Figure 31 CFD results compared to clean experimental data

The correlation between CFD and experiment is disrupted when the data is tripped. Arguably, CFD should be closer aligned with the tripped solution because the turbulence models assume a turbulent boundary layer from the leading edge. This does not appear the case. One explanation is that the trip strip is altering the boundary layer in a way that is not normally seen for this shape at this Reynolds number. The definitive answer to this question remains unknown.

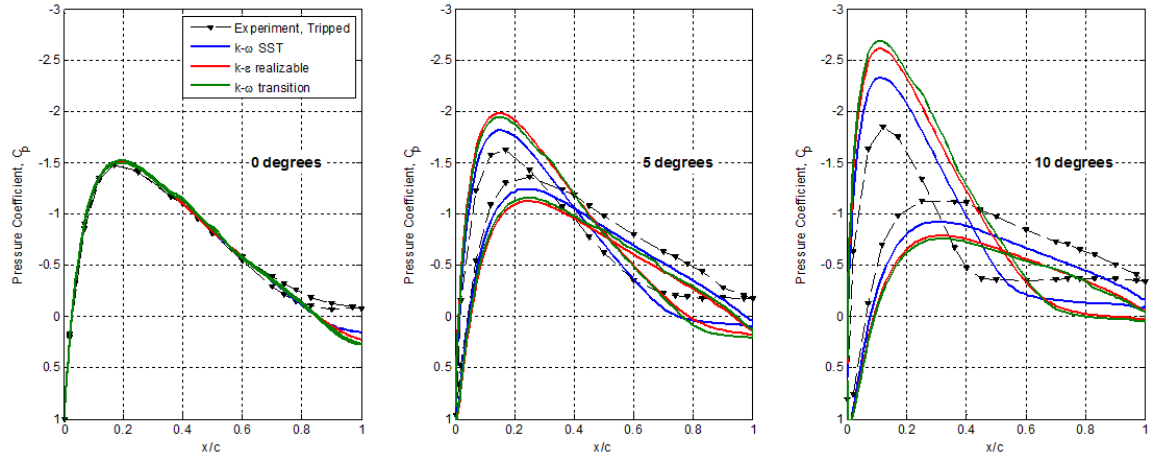

Figure 32 CFD results compared to tripped experimental data

Figure 33 and Figure 34 show velocity contours and vectors from the CFD solution using the k-ω turbulence model.

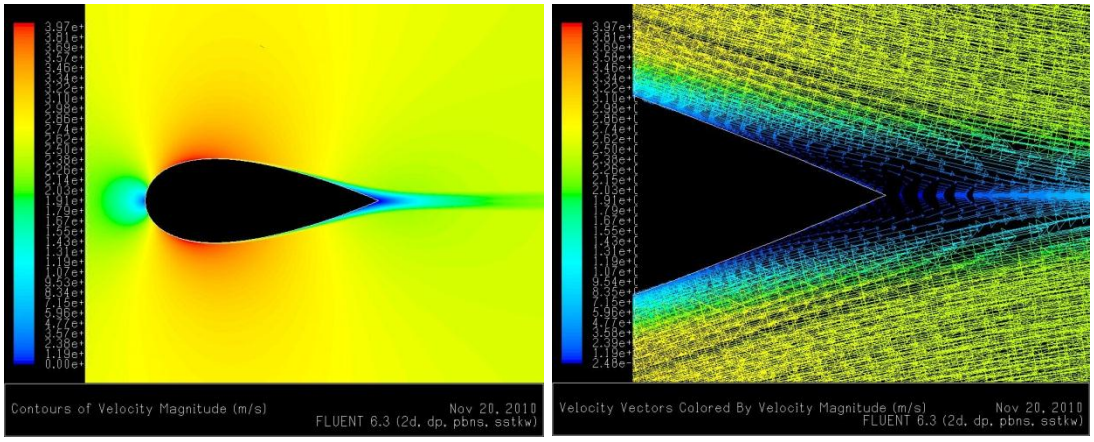

Figure 33 Contours of velocity and velocity vectors on NACA 0036 at 0° angle of attack with k-ω SST

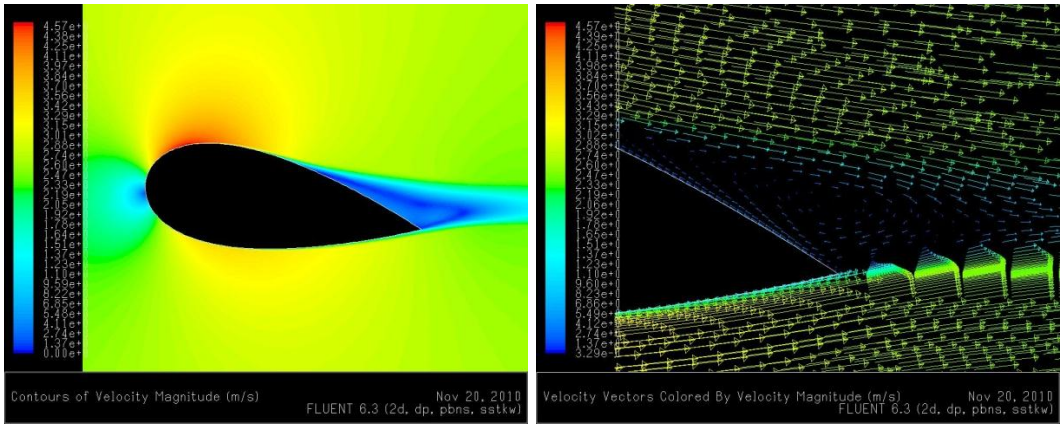

Figure 34 Contours of velocity and velocity vectors on NACA 0036 at 10° angle of attack with k-ω SST

Figure 35 plots the experimental uncertainty for the k-ω SST model along with numerical uncertainty resulting from spatial discretization determined from a mesh independence study for the airfoil at 10° angle of attack. The error bars show that the CFD is capable of predicting all pressures with accuracies within experimental uncertainty except the area

leading up to the point of separation. The error bar is very large at the onset of separation, signifying the high oscillations seen in the solution at that point.

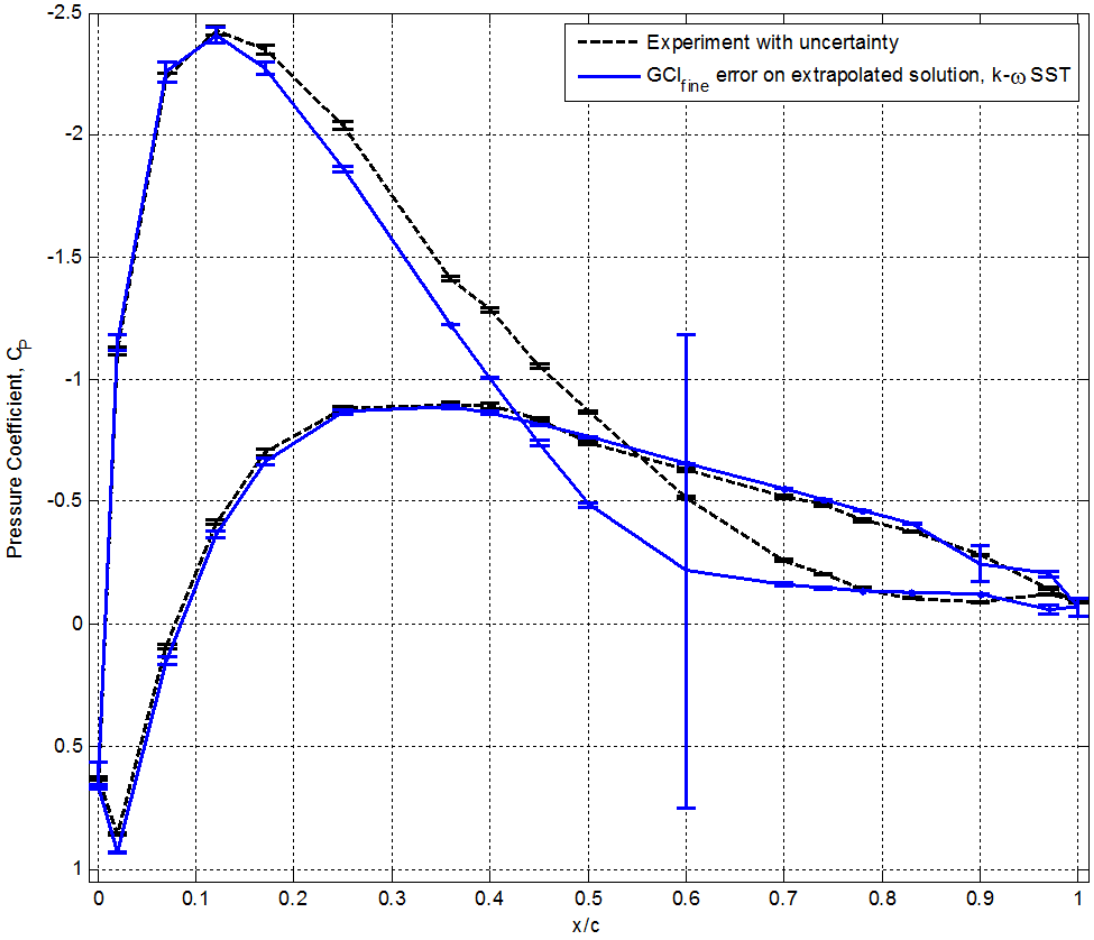

Figure 35 Experimental error compared to CFD discretization error

Force data for the CFD runs can be seen in Figure 36. Drag shown is only the pressure component of drag without skin friction drag to properly compare to experimental data. Lift does not equal zero at zero degrees as a result of minor model problems, which was explained previously in the model description in section 3.2.

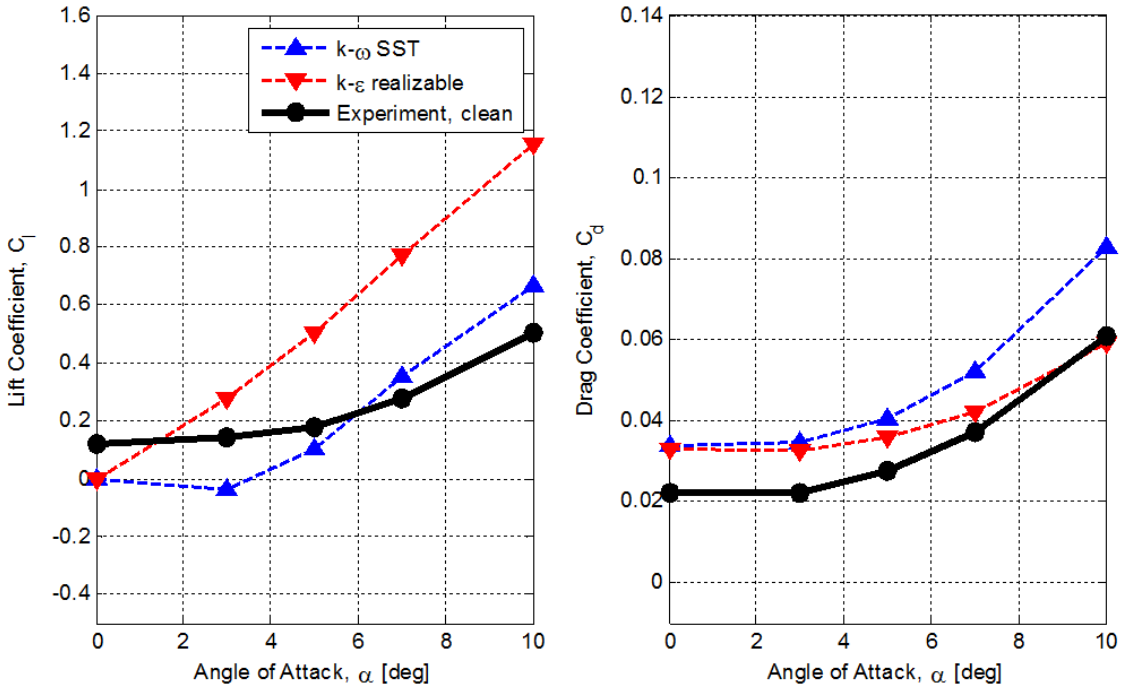

Figure 36 Force results from CFD simulation

Although under-predicting the separation point, the k-ω SST turbulence model shows fair correlation with experimental force data. It correctly models the initial flat slope of the lift curve and rises at around 5 degrees, only too abruptly. The drag is incorrect in magnitude but captures the trend extremely well. The k-ε realizable does not capture the non-linearity of the lift slope– an important flow feature of the NACA 0036. It also does not follow the trend of the drag curve.

CFD simulation was also run for the case of a 2% Gurney flap. The results are shown in Figure 37. Trends of larger negative pressure peaks and lower negative pressures of the lower surface are over pronounced in CFD. This signifies that in addition to not predicting separation correctly, CFD is also over-predicting the effect of the Gurney flap. At 10 degrees, problems arise around the trailing edge region, indicating problems in meshing or convergence. This also resulted in highly irregular force plots which are not

shown. Perhaps large cell volume change is responsible for some of the added error in the solution. More work must be done in meshing as well as modeling for adequate correlation of Gurney flap CFD to experimental data.

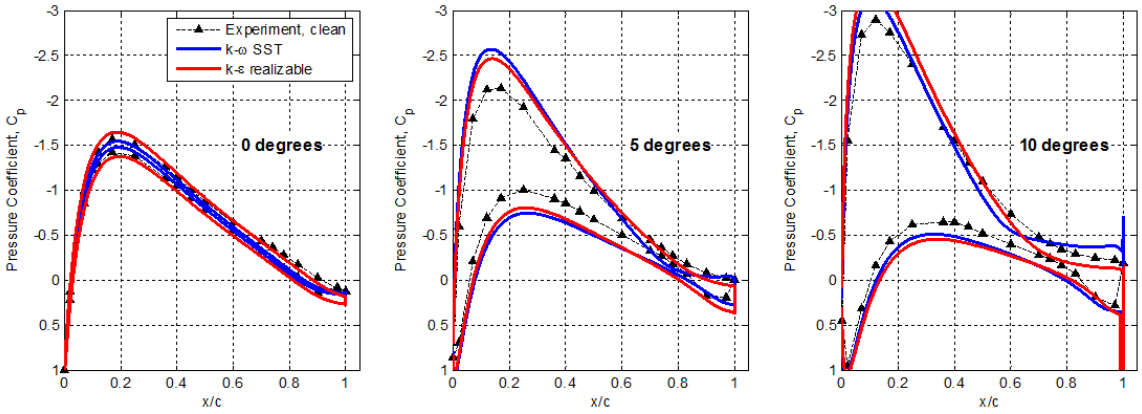

Figure 37 Comparison of CFD to experimental pressure data of NACA 0036 with 2% Gurney flap

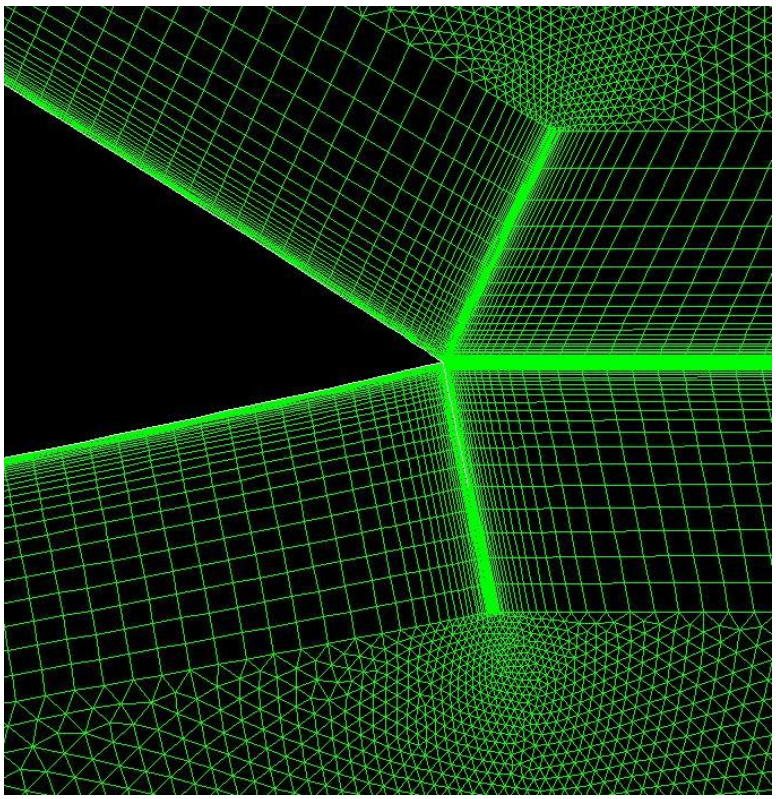

Figure 38 Mesh detail of Gurney flap

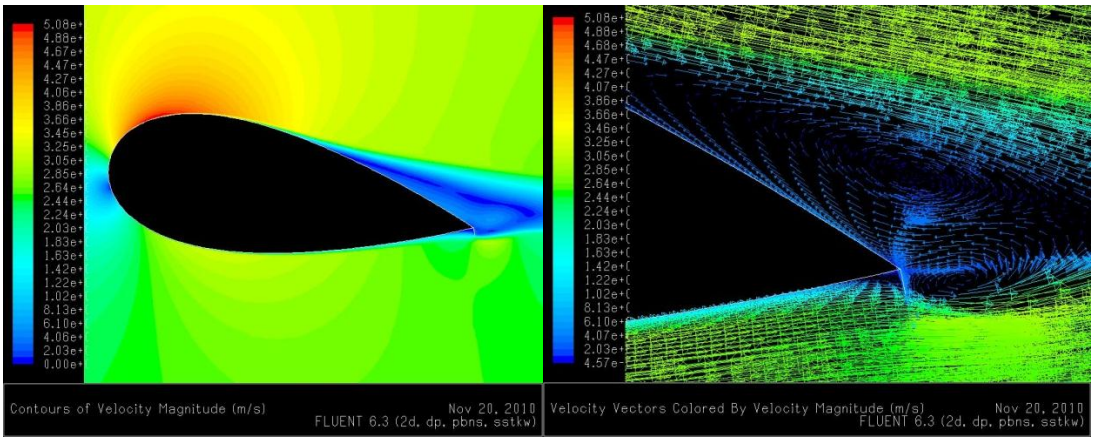

Figure 39 Contours of velocity and velocity vectors of NACA 0036 at 10° angle of attack with a 2% Gurney flap, using k-ω SST turbulence model

7 Final Remarks on Research

7.1 Conclusions

After significant work in repairing the Cal Poly low speed wind tunnel, fair correlation with previous data was achieved. Correlation is as close as possible without more information on the specifics of each previous test. However, much more work is necessary in order to improve the data quality and repeatability of the wind tunnel data which is outlined at the end of the next section.

The effect of the Gurney flap was to lower the peak pressures on the upper surface and raise the pressures on the lower surface. This resulted in a straightening of the lift curve slope, eliminating the lift reversal phenomenon. In addition, small but significant drag decreases can be seen at small angles of attack, ranging from 4-27% of form drag; however, these are quickly diminished as angle of attack is increased to 3 degrees or more, limiting their possible application. Also, increasing Gurney flap size increased the lift to drag ratio.

Attempts to simulate the flow field with 2D Reynolds averaged Navier-Stokes (RANS) CFD were marginal. Mentor's $k-\omega$ SST eddy viscosity model proved the most accurate, with only slight error in over predicting separation. However, the tripped boundary layer proved too difficult to model. CFD modeling of the Gurney flap was inadequate, with the CFD over predicting the effect of the flap seen in the experiment.

7.2 Future Work

Future work on the experimental side of the research could involve trying to increase the drag benefit of the Gurney flap. The effect of a double-sided Gurney flap (T-flap) might result in a wider band of drag benefits in angle of attack, with straighter lift curve slopes for better controllability. Surface flow visualization such as China clay, tuffs, or florescent oil would also be helpful to better understand the flow physics.

For the CFD simulation, there are many new ideas to explore; many of which are eliminating assumptions previously made with the current simulation. Because the separation was not modeled correctly, assumptions simplifying the separation would be the primary focus. One idea would be to try an unsteady simulation. Figure 40 shows smoke visualization performed on the NACA 0036^3 which clearly shows unsteady vortex shedding. Eliminating the steady state assumption might capture this effect. Another idea would be to model the flow in 3D. Figure 41 shows the 3-D separation pattern between the junction of the model and the wind tunnel walls. With an aspect ratio of only 2, these effects might have influenced the flow field along the centerline, where pressure measurements were taken. Finally, if these methods prove unfruitful, then higher fidelity turbulence modeling would be required, such as higher-order eddy viscosity model such as v^2-f, or going beyond Reynolds averaging to Large Eddy Simulation (LES). Before embarking on such complicated modeling techniques, this author would recommend first cross-checking the accuracy of the current experimental data with alternate wind tunnels. This demonstrates the ever-present challenge of matching aerodynamic experiments to numerical simulation.

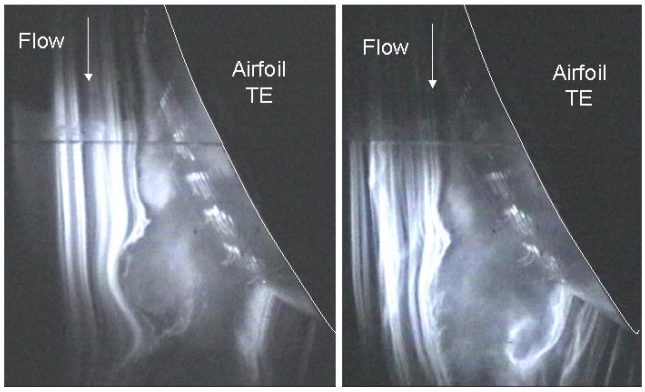

Figure 40 Unsteady vortex shedding seen in smoke visualization[3]

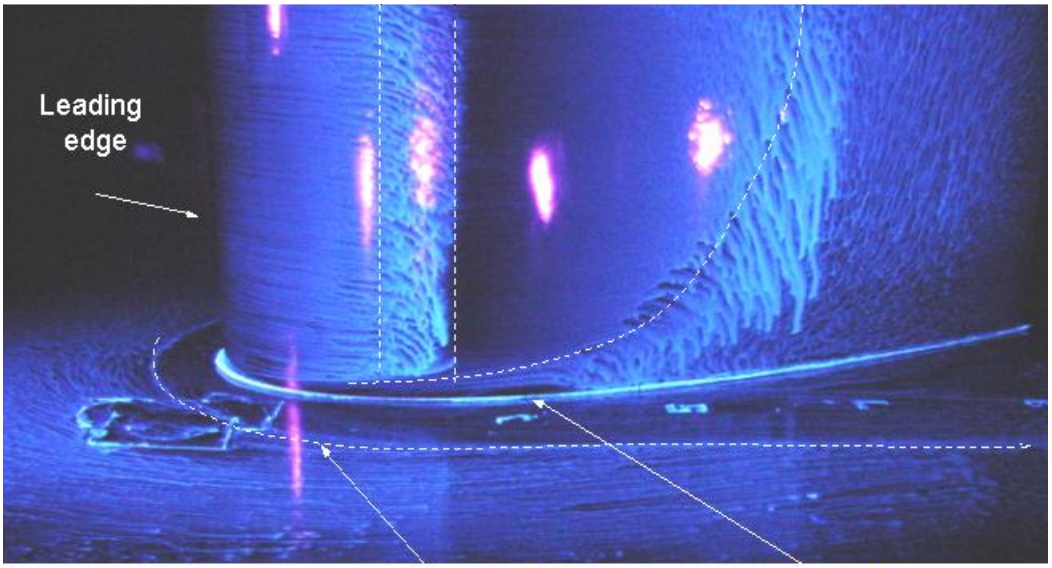

Figure 41 3-D separation of the junction between the model and wind tunnel walls[3]

8 Wind Tunnel Facility Investigation

A collaborative effort by Greg Altmann and Joshua Roepke

8.1 Discovery of a Problem

After looking over several data sets, a problem was seen with the wind tunnel data. The best way to describe what was happening was abnormal blockage effects. This was readily apparent in three data sets: the 2D cylinder used in the Aero 307 lab class, the 2D NACA 4412 airfoil also used in the Aero 307 lab class, and the NACA 0036 airfoil used in two masters' theses. For the cylinder, the pressure peaks observed were much higher than those predicted by the theoretical inviscid pressure distribution. Normally, this would be attributed to wall blockage effects. Wall blockage effects are when the model and the wall are close enough together to cause an increase in acceleration of the flow that would not otherwise be seen. The flow between the cylinder and the wall is being restricted and made to accelerate more than it would if no walls were present. This accelerated flow is seen in the data in the form of lower pressures as seen in Figure 42. In these cases, the wall was originally thought to be too close to the cylinder and a smaller model should be used. However, this same effect was viewed again with the NACA 4412 airfoil, only for this case it was compared with a CFD simulation which included the wind tunnel walls in the model. The CFD run with walls did not change from the solution run without walls, but the experimental data still showed the blockage problem, as can be seen in Figure 43. When comparing the NACA 0036 model data to NASA experimental data a similar effect was observed, as can be seen in Figure 44. All of this evidence led to the following investigation.

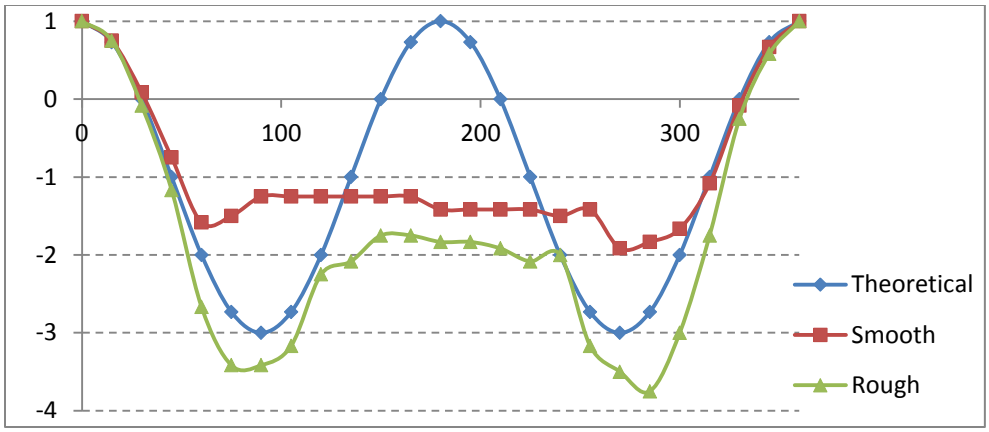

Figure 42 Cylinder C_p data with high negative peaks

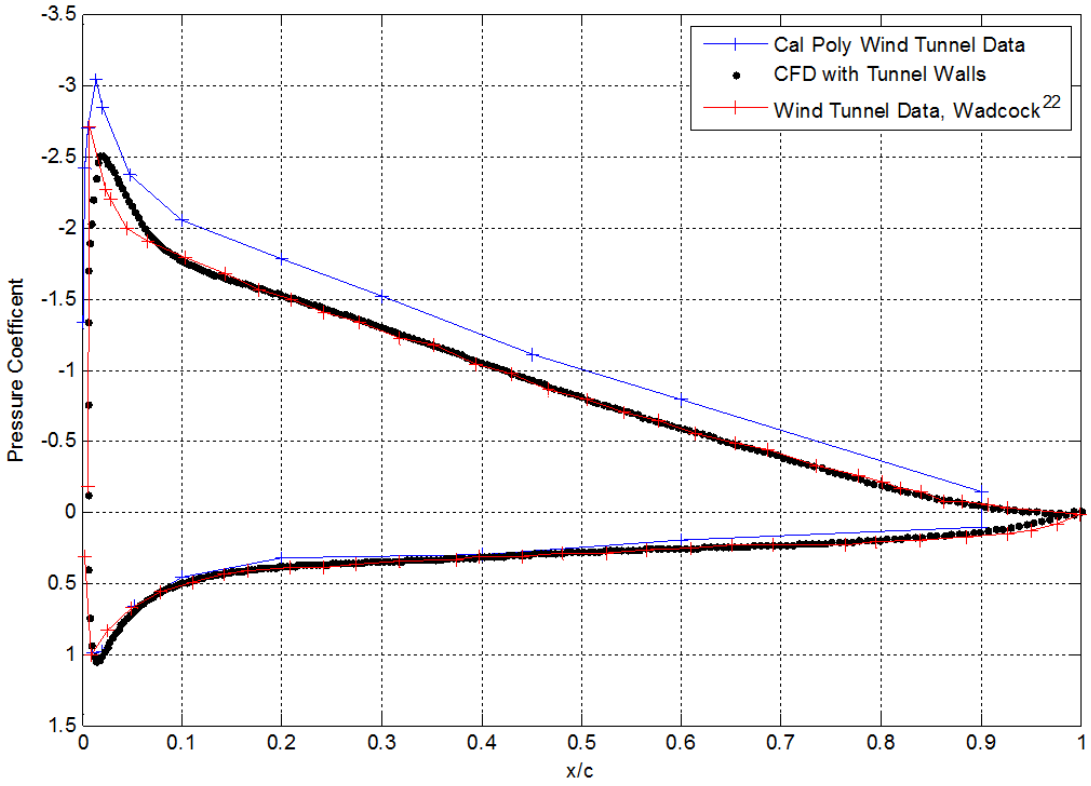

Figure 43 NACA 4412 airfoil at 8° angle of attack compared to a 2D CFD simulation with wind tunnel walls modeled and NASA wind tunnel data[22]

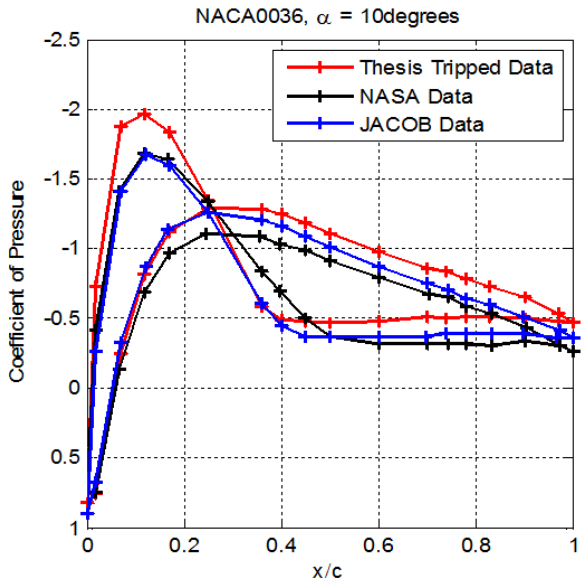

Figure 44 NACA 0036 data compared with NASA data[3] taken in the same size tunnel cross-section and older Cal Poly Data (Jacob Wilson[5])

8.2 Wall Boundary Layer Measurement

The first theory as to why the data looks as it does was abnormally high boundary layers on the wind tunnel walls. The idea was that the boundary layers were taking up a large amount of the space between the walls and wind tunnel models and reducing the area that the freestream air can flow through, and this restriction was causing the flow acceleration which lead to the lower than expected pressures on the surface of the models. To test this idea, a total pressure probe mounted on a traverse was built to fit into a panel space on the wind tunnel. The traverse and equipment can be seen in Figure 45.

Using this device, boundary layer measurements could be taken wherever there was an access panel. A Velmex 10" traverse was used with movement precision up to 0.00025", and a 1/32"OD Pitot tube. Matlab was used to automate the probe measurements through the use of a Graphical User Interface (GUI) as seen in Figure 46. The GUI allowed the user to do many manual or automatic operations. The manual operations included the

ability to reset the position of the probe, set a step size, and step the traverse in both directions. The automatic operation was meant for the automatic capture of the pressure data from the Scanivalve, converting this data to dynamic pressure, and plotting this in the form of a boundary layer profile. Especially useful was the ability to specify the heights off the wall that the probe would capture data. This allowed the user to resolve important flow features while keeping measurement time to a minimum.

The probe dimensions can be seen in Appendix B. The diameter of the probe head was chosen to allow measurements as close as possible to the surface of the tunnel. The 1/32" OD tubing was the smallest size that was felt to be rigid enough to not deflect under a 35 m/s freestream velocity. The probe was manufactured to take advantage of the long 10" of travel that was available with this particular traverse system.

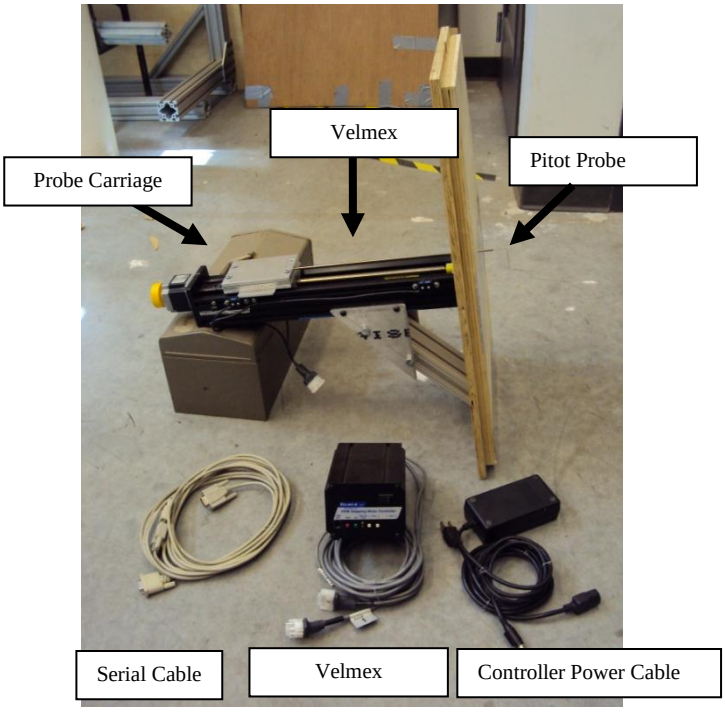

Figure 45 Traverse support panel constructed to measure wall boundary layers

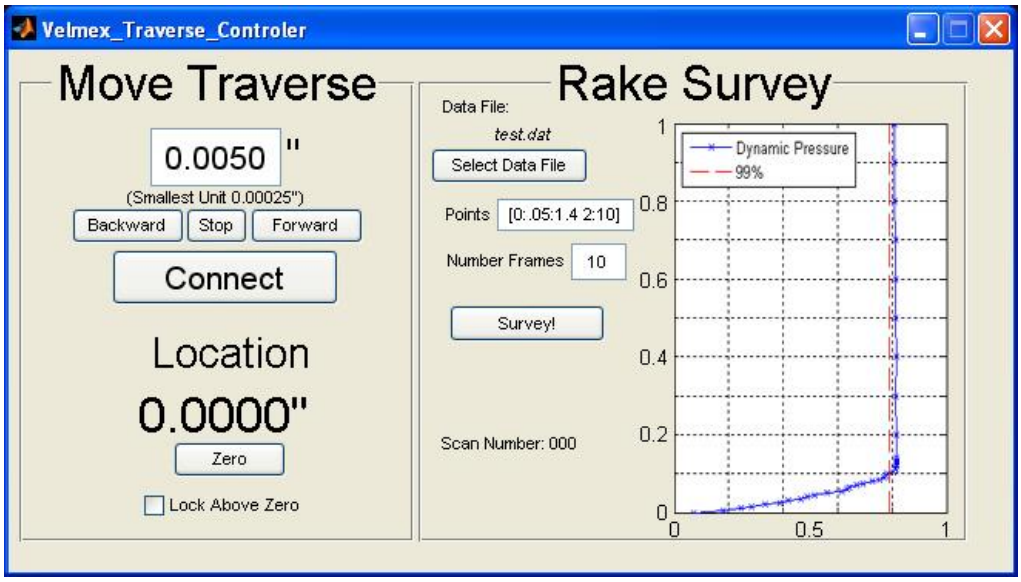

Figure 46 MATLAB GUI for traverse system

Two sets of data were taken with the probe mount. First, all four walls were measured just behind the inlet. These profiles can be seen in Figure 47. After this test, it was determined that strange behavior was observed in the flow direction along the floor and ceiling walls. This led to the second survey, which was along the bottom wall. The bottom wall was investigated instead of the ceiling wall because the floor has more removable panels, i.e. measurement locations, than the ceiling. For these tests, all joints upstream of the measurement were sealed with silicone calking to be sure leaks were not causing the disturbance. Many small and large scale leaks had been detected and fixed and this made almost no impact on the disturbance seen in the boundary layer profiles. Therefore leaks were removed from the list of possible sources of the disturbances.

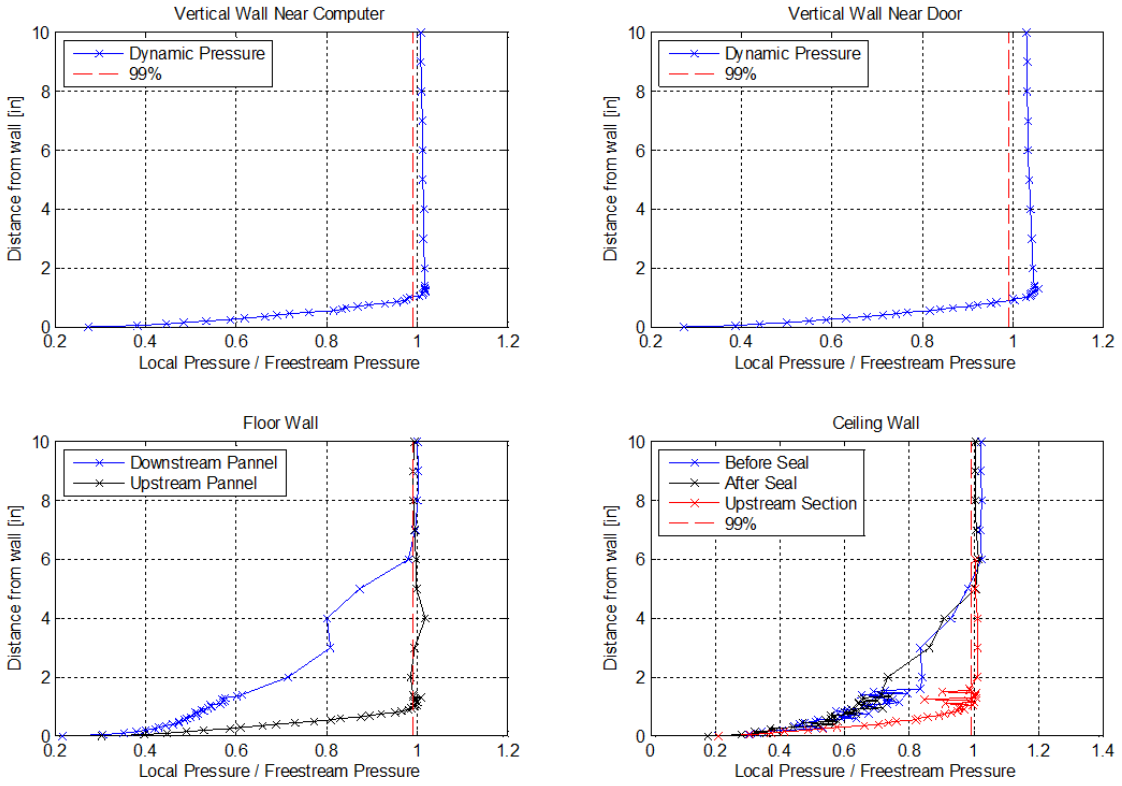

Figure 47 Boundary layer measurements over all four walls. On the "floor wall" graph, "Downstream" corresponds to panel 2, and "Upstream" refers to panel 1 (in the following figure). For the ceiling measurements, "Upstream" corresponds to 2.5' from the inlet, and before and after seal measurements were 7.5' from the inlet at the same location. (Local dynamic pressure/freestream dynamic pressure; q/q_∞)

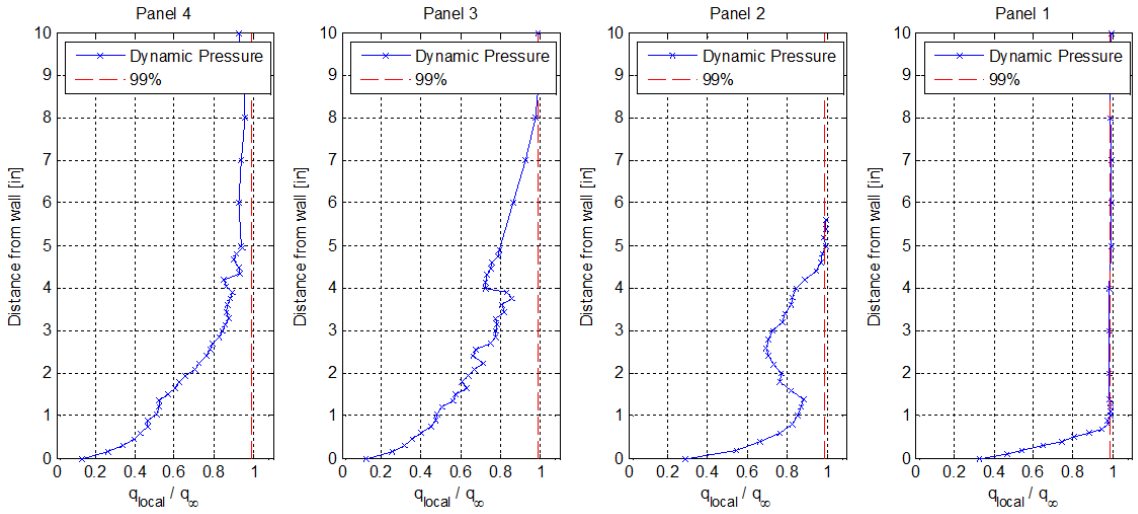

Figure 48 Boundary layer measurements along the floor of the wind tunnel. Panels 4, 3, 2 and 1 are 9', 7.5', 4', and 1' away from the inlet respectively.

The boundary layers on all panels within 2.5’ from the inlet are fine. The vertical walls have very clean profiles and show no problems except a higher than normal dynamic pressure, but no measurements were taken downstream to verify that no problems develop. The horizontal wall boundary layers grow much quicker than they should and have highly erratic behavior. It was thought that the abnormal boundary layer profiles were caused by flow problems in the inlet that might even include separated flow in the inlet. This led to an investigation of the inlet contracting section in the inlet.

8.3 Smoke Visualization

To gain insight into what is happening in the inlet, streaklines were created with a smoke machine starting from outside the screens. An observer would then stand in the inlet while the tunnel was on to take pictures and/or video. The smoke generator was not the lab’s smoke wand, but a commercial “Fog machine” smoke generator. This allowed for a thicker stream of smoke, which was more useful for this study. The following pictures show some peculiarities.

Figure 49 Smoke visualization inside the inlet

For both bottom corners of the tunnel, the streakline was pushed to the center of the wind tunnel. It also was pushed upward toward the center of the tunnel almost hitting the sting balance when reaching the last test section. As the smoke machine was moved up along

the vertical edge, the streakline shifted across the bottom wall of the wind tunnel until the smoke machine was about three to four feet high, when it then aligned with the bottom left corner of the test section. This can be seen in the far left picture of Figure 49. As the smoke machine was raised along that vertical edge, the smoke stayed close to the vertical wall in the test section, as would be expected for uniform flow. The top corners did not have this strange behavior. A streakline released from the bottom center would rise very high, and would not follow the bottom wall of the tunnel. This was interpreted as possible separation, even though a recirculation zone was not seen with the smoke. This can be seen in the far right picture of Figure 49.

8.4 Oil Visualization

At first, the peculiar behavior of the inlet was attributed to poor inlet geometry. Oil visualization was used to investigate the possibility of separation in the inlet. For this experiment, white Mylar was taped to the throat of the inlet, and a mixture of 100 centistoke oil (SAE 30) and dry graphite lubricant, for visibility, was brushed over the surface. This did show a line of separation near the inflection point of the inlet. It was not an even or straight line, but it did show that the oil was pooling up at that location, most likely a result of reversed flow. As can be seen in Figure 50, the entire centerline of the tunnel through the first test section was covered with Mylar and oil flow was done and no reattachment point was found. A trip strip was added to try to trip the flow to turbulent in an attempt to energize the boundary layer and keep it attached. This was unsuccessful and resulted in a line of separation in the same location as before. Ideally, the oil upstream of the separation line would have been pushed in the direction of flow while the oil downstream would have been pushed opposing the direction of flow as is

characteristic of a recirculation region. Unfortunately, this was not the case because the tunnel wall in the area of interest was heavily sloped. Between the time that the tunnel had shut down and the technicians could get inside to document the results, the oil had run down the slope in the upstream direction. As a result, no flow direction could be found from this visualization. Looking at the smoke lines, no sudden breakaway of boundary layer is seen.

Figure 50 Flow visualization showing oil pooling in the throat (before and after)

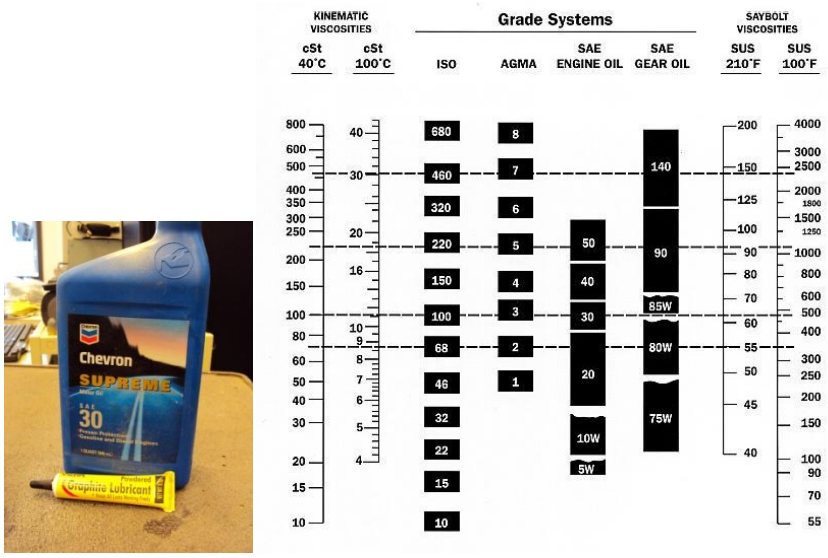

Figure 51 Materials for oil visualization and conversion chart for oil viscosities

8.5 Initial CFD Investigation

At this point the inlet geometry was thought to be the problem because of the apparent separation. A CFD study was performed to determine whether separation was predicted in the inlet. One corner of the inlet was measured in 3D coordinates, then modeled in Solidworks, meshed in ICEM and solved in Fluent. A structured mesh was used because of geometric simplicity with a y+ of less than 1 on the walls. The k-ω SST turbulence model was used for its ability to capture separation accurately. For the first case, two lines of symmetry down the center of both walls were drawn to reduce cell count, leaving only one quadrant. The following images show the result of this study.

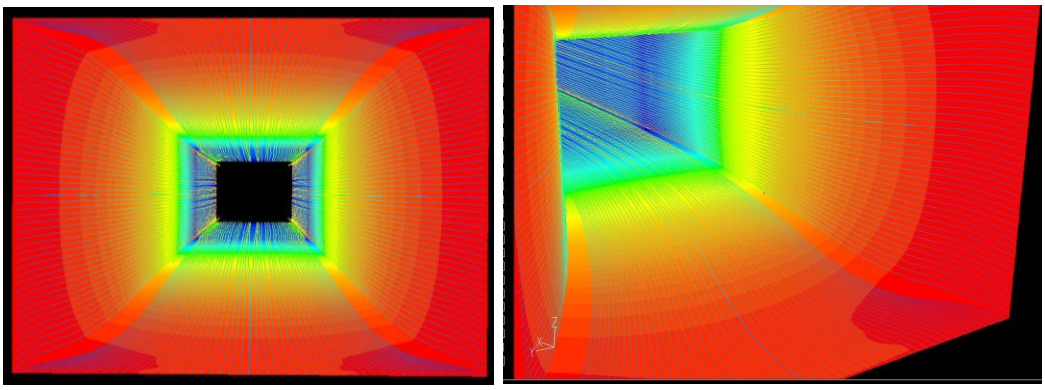

Figure 52 Preliminary CFD study. Streaklines colored by velocity with contours of static pressure on the walls. Symmetry lines are mirrored

Figure 52 shows small problems in the corners of the wind tunnel, but no major issues exist. On the image to the left, separation is visible in the corners of the test section, but not enough to disturb any 2D airfoil sections. Also, importantly, no separation was predicted at the throat, contrary to our latest theory. The streaklines also did not match those seen with the smoke visualization. At this point, the differences between the CFD study and the real tunnel were thought to be the true source of the problem. Of those, the assumption of a uniform inlet velocity seemed to be the poorest assumption. This created a need for inlet velocity measurements. Lastly, this indicated that if we could get a uniform velocity profile at the inlet, the geometry of the contraction would probably be sufficient for uniform flow in the test section.

8.6 Inlet Velocity Measurements

For this experiment, a Pitot-static tube was used to measure inlet velocity behind the screen. Reproducibility for the data proved to be challenging as the normal method of acquiring this data, a traverse of some sort, would be very expensive in an area that is 12' wide and 9' tall. Initial data showed high sensitivity to movements of the probe, and distance away from the screen. To alleviate some of these issues, the probe was mounted

to a piece of 1”x2” timber with a spring loaded clamp as can be seen in Figure 53. Using this method, measurements were fairly reproducible. Each set of measurements was taken twice to verify accuracy, with each data point averaging 15 frames with 100 scans per frame. Measurements were taken across both centerlines every foot, and six additional measurements were taken in each quadrant. The actual measurement points can be seen in Figure 55 as black crosses.

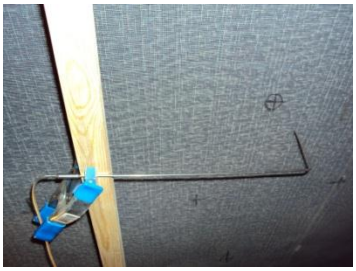

Figure 53 Configuration for velocity measurements

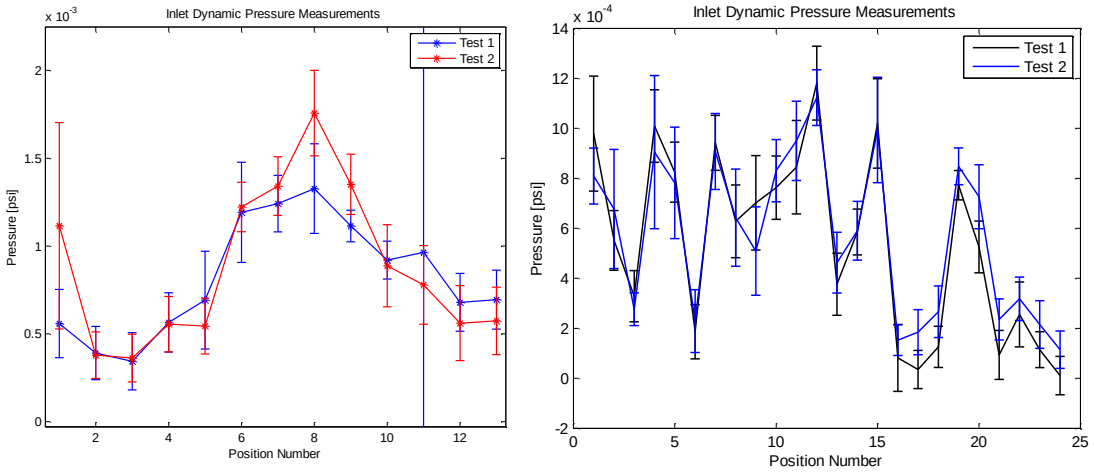

Figure 54 Plots showing the repeatability of the measurements on the vertical centerline (left) and horizontal centerline (right)

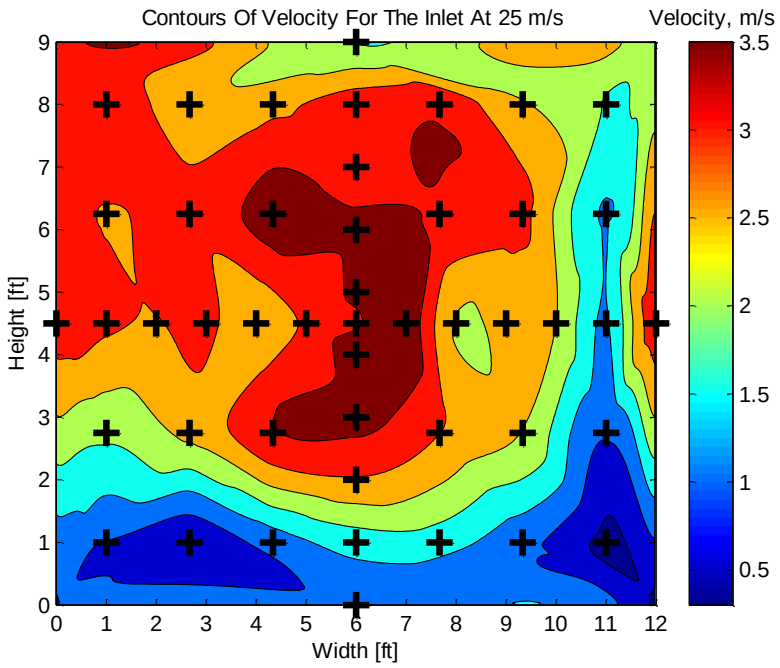

Figure 55 Contours of velocity in the inlet, downstream of all screens and honeycomb. The black "+" are the points of measurement inside the tunnel.

This data showed high non-uniformity, and much slower velocity towards the ground and on one side. In the room of the wind tunnel, the defect was on the side of the room with the exit door. A certain degree of non-uniformity at the inlet is expected. The expected profile should show a slightly larger velocity in the center section of the inlet with low velocity close to the walls because of the friction of walls slowing down the flow in those regions. The magnitude of the velocity variations that were measured were on the order of 200%-350%, which is considerably more than expected.

After taking this data, the velocity data was imposed onto the inlet boundary condition in the CFD to determine if this would reproduce what was happening in the wind tunnel. Symmetry was no longer utilized in the CFD solution because of this non-uniform velocity profile. The new CFD results matched extremely well to streaklines viewed with

smoke in the inlet. This confirmed that the inlet geometry was not the major problem, but the inlet velocity was the problem.

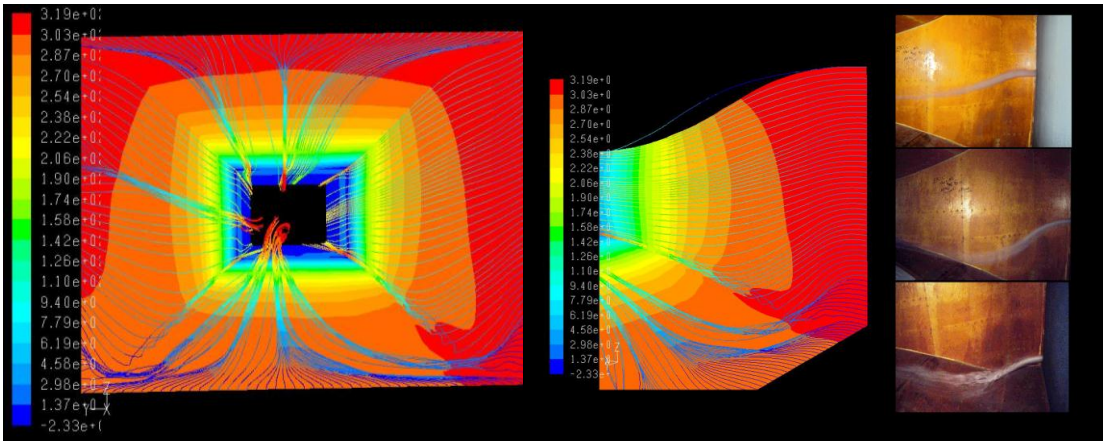

Figure 56 CFD case with measured velocity imposed on the inlet boundary

8.7 Inlet Diagnosis

Once it was determined that the inlet velocity profile was the fault of the non-uniform flow problem, the source of the non-uniform inlet velocity profile was sought. Initially, the source of this problem was thought to be the inability of the air coming from the roof vents to reach the lower portions of the tunnel inlet. This idea proposed by Dr. Tso was tested by putting a splash shield below the inlet vents to force the flow to "splash" around the shield. This would force the air to take a longer path to the inlet and would, therefore, have a better chance of making it to the lower portions of the inlet. This test failed to produce any noticeable change in the smoke streamlines in the inlet.

The second theory was that the air entering the room was restricted. This is obvious when one compares the inlet size of 108 ft^2 to the roughly 36 ft^2 of the roof vents. These vents might not have been letting in enough air. The inlet creates a low pressure region directly in front of it which was drawing in air from not only the roof vents, but also the

large exit door. It is a common occurrence that when the tunnel is set above 20 m/s, air is felt coming in from this exit door toward the tunnel inlet. The thought was that this flow, when it reached the inlet and tried to turn 180°, was disturbing the flow from the roof and this disturbance resulted in the distinct non-uniform flow pattern in the inlet. This flow from the exit door could not make the 180° turn and was trying to enter the straws at such a large angle that the straws were "stalled" which resulted in their inability to accommodate as much air as they normally would, thus acting as a restriction. To test this theory, the side doors of the wind tunnel room were opened allowing a large amount of air to enter through them. This would surely create a different flow pattern in the room and would change the inlet disturbance pattern. But, no changes in the streamlines in the inlet were observed.

Next, the inlet itself was investigated. Initially, it was thought that the inlet should not be clogged because there was still smoke going through the straws and light could be seen when a flashlight was shown through them as well. In spite of this, a quick blast of pressurized air showed a large plume of dust and dirt coming out of the straws both on the inside of the flow straightener and on the outside. A noticeable change in color was observed when the dirt was blown off of the straws. After a thorough cleaning of the inlet from the outside, further smoke flow visualization was done to qualitatively evaluate the change. These results can be seen in Figure 57 and Figure 58. The cleaning produced a marked improvement, but the problem still existed, just to a lesser extent. To test this promising theory that the straws were just clogged, a restriction was made out of cardboard to simulate the clogged straws. The cardboard had 2"-3" holes cut in it and spaced roughly every 4"-5" on center in a semi-regular pattern. This restriction was

placed in front of the top corner of the inlet where no unusual flow patterns were previously observed and smoke visualization confirmed that the flow irregularity had been reproduced. This confirmed that the flow irregularities in the contraction were the result of restrictions in the flow straightener. Next, cleaning was done on the inside of the inlet. This consisted of trying to blow, with compressed air, the dirt out from the inside of the tunnel.

Figure 57 Smoke flow visualization before cleaning

Figure 58 Smoke flow visualization after cleaning. Also visible is the dirt and dust that was removed during the cleaning process

After further inspection, a thick layer of dirt and debris was observed between the straws and the 2nd screen. This layer of blockage was difficult to remove due to the 3rd and 4th screen being behind the 2nd screen. To clean this blockage out thoroughly, the removal of

all of the straws was needed. It was also concluded that the replacement of the straws was needed to ensure their cleanliness. Upon pricing of replacement straws, it was decided that a better solution was to replace the straws with honeycomb, a much more traditional material for a flow straightener.

8.8 Honeycomb Selection

To determine the required size of the honeycomb, many sources of information were consulted. In these sources, the important parameters for the selection of the honeycomb was the pressure drop coefficient, K, the actual cell hydraulic diameter, D_h and the L/D_h ratio of the cells. The pressure drop across the flow straightener is important to ensure that the new flow honeycomb will not pose a larger restriction on the inlet than the straws. If the honeycomb had a larger pressure drop across it, the fan would have to expel more energy to produce a given speed in the test section and the maximum speed of the tunnel will be reduced. Equation 8-1 was said to be the most common[12] one used; therefore, it was used here.

$$K = \lambda\left(3 + \frac{L}{D_h}\right)\left(\frac{A}{A_{flow}}\right)^2 + \left(\frac{A}{A_{flow}} - 1\right)^2 \qquad 8\text{-}1$$

$$\lambda = 0.375 * Re^{-0.1}\left(\frac{\Delta}{D_h}\right)^{0.4} \qquad Re = \frac{V\Delta}{\nu} \leq 275 \qquad 8\text{-}2$$

$$\lambda = 0.214 * \left(\frac{\Delta}{D_h}\right)^{0.4} \qquad Re = \frac{V\Delta}{\nu} > 275 \qquad 8\text{-}3$$

A summary for the sizes and pressure drop values for the proposed honeycomb sizes can be seen in Table 4. As mentioned in the literature, the honeycomb is the best at reducing the transverse turbulence. It does this by literally dividing the turbulence into small

disturbances the size of the honeycomb cells as the turbulence is drawn into the honeycomb. But the honeycomb produces turbulence as well as destroys it. Care must be taken to ensure that the production of turbulence by the honeycomb is minimized by limiting the boundary layer growth. The longer the cell, the larger the boundary layer inside it and the larger and stronger the turbulence will be that is produced by the cell. The general rule is that the cell must have an L/D_h in the range of 6-8[2]. In these equations, *T* is the material cell wall thickness. For the derivation of Equation 8-5, see Appendix D. For the Matlab code that performs the calculation for Table 4, see Appendix E. All flows in nature contain turbulence. But if the turbulence intensity is low enough, we can consider them as laminar. For our case, because of the flow path, the turbulence intensity is not low enough to classify the flow as laminar.

Table 4 Summary of straws and proposed honeycomb sizes

Material	**D_h** (in)	**L** (in)	**L/ D_h**	**Wall Thickness (*T*)** (in)	**A/A_{flow}**	**K**
Straws	0.219	7.75	35.4	0.006	1.09	1.66
HC	0.25	2.0	8	0.002	1.02	0.40
HC	0.125	1.0	8	0.002	1.04	0.55

$$K = \frac{\Delta P}{\frac{1}{2}\rho V^2} \qquad 8\text{-}4$$

$$\left(\frac{A}{A_{flow}}\right)_{circles} = \frac{{D_h}^2}{{D_h}^2 - \pi(D_h T - T^2)} \qquad 8\text{-}5$$

$$\lambda\left(\frac{A}{A_{flow}}\right)_{Hexagons} = \frac{D_h}{D_h - \frac{8}{3}T} \qquad 8\text{-}6$$

The only general rule that could be found for the sizing of the honeycomb was that the cell size "shall be smaller than the smallest lateral wavelength of the velocity variation"[23]. The problem is that the upstream velocity and turbulence data is not available for this

open circuit tunnel as it is for a closed circuit tunnel. Even if it were available, with an in-draft tunnel such as ours with the in-flow coming from the atmosphere, the incoming flow could vary considerably day to day, depending on the atmospheric conditions such as wind and temperature. Unless measurements were taken over a considerable time span to capture variations mentioned above, the above data would not be very useful. Therefore, based on the above calculations, it was thought that the smaller celled honeycomb would be best for our inlet. This was because the pressure drop coefficient was still 3 times less than that for the straws and would reduce the turbulence levels in the transverse directions by a factor of 1.75. Also, by choosing the correct L/D_h, the amount of turbulence produced by the honeycomb would also be reduced considerably. This should result in a large net reduction in turbulence over the current straws.

Other secondary items such as soiling/fouling, susceptibility to suffering permanent damage, mounting difficulties, and price were also considered in the honeycomb selection. Soiling and fouling were important because it appears as though the current state of affairs was brought on by soiling and fouling of the straws and screens without an adequate way to clean them. To prevent this from happening again, the inlet will be designed with the ability to clean both sides of each screen and the honeycomb.

The materials that were evaluated were Nomex, Kevlar, and aluminum. After samples were received of the three materials, it was believed that the Nomex would be susceptible to fouling because of the surface "fuzziness" that was apparent at the entrance and exit to the cells. Of the aluminum and Kevlar sample, the aluminum was thought to be susceptible to permanent damage. The Kevlar displayed a good degree of resiliency when the cells were subjected to harsh handling. Susceptibility to damage was important

because, downstream of local damage in the honeycomb, the turbulence level can increase up to 3 times that of the average freestream value[24]. For these reasons, Kevlar seemed to be the best choice, but on the receipt of price quotes for the material, it was deemed too expensive. Polycarbonate honeycomb was used because it was a good compromise with all of the requirements, and was very cost effective.

8.9 Screen Selection

Incoming flow contains turbulence on a larger scale than the openings in the screens. The flow is restricted and drawn through the screens by a driving pressure force supplied by the fan of the wind tunnel. The wire of the screens acts like small subcritical cylinders in the flow. The flow separates before it reaches the maximum thickness of the wire. This separation breaks down into turbulence, leaving the honeycomb as smaller-scale turbulence. The small-scale turbulence then dissipates at a much higher rate as it is closer to the Kolmogorov scale in which turbulence is small enough to turn to heat. Because of the previously mentioned lack of upstream turbulence information, the actual turbulence inside the test section cannot be estimated accurately. When the wind tunnel was housed in the hanger (Building 4), the turbulence intensity was measured and found to be 0.5%. No information is available as to what tunnel speed this test was conducted. It is unknown if the test was performed in the longitudinal or transverse direction, or even how accurate the test is believed to be or what method was used to obtain the measurements. This is also, presumably, conducted when the straws were clean. If these conditions were known, the upstream flow turbulence condition could be found and used as a reference to estimate the test section turbulence in its current state. Turbulence levels below 0.1% are considered acceptable and levels below 0.05% are required for any

kind of laminar flow research[25]. But because 0.5% has been deemed an adequate turbulence level by the overseer of the wind tunnel, Dr. Jin Tso, no significant reduction of the turbulence below this level will be sought. Before repairs, there were four screens which all had a mesh size of 18 openings per inch in each direction. This is referred to as an 18 mesh screen. The first two screens were just in front and behind the straws and used to hold the straws in place. This was followed by a gap of about 1.5" between the second and third screen and the same gap between the third and fourth screens. The new screens just before and after the honeycomb are still 18 mesh screens. The last two screens get progressively finer with the third screen being a 22 mesh screen and the last screen being a 26 mesh screen.

Another important design aspect is the open ratio of the screen. This is defined in a similar manner to the A/A_{flow} ratio for the honeycomb sizing. It is the ratio of the open area in cross section of the screen to the area of the opening that holds the screen. The open ratio should be at least 57%[22]. Below this value, the jets of air that go through the small screen openings start to form instabilities in the flow and actually produce more turbulence. For this reason, an open ratio of between 64% and 72% will be maintained for all screens.

Many general rules for the spacing of the screen have been given, but few can be implemented into the current inlet design because they would make the inlet too long. The general rule is that the screen should be spaced at least 0.2 times the settling chamber diameter[22]. For our inlet the settling chamber diameter is equal to the hydraulic diameter of the inlet, which is 10.28 ft. This would require a screen spacing of 2.06 ft. This is not possible because it would require the addition of about 4 ft to the length of inlet. A

second general rule for screen spacing is that they should be at minimum 25 divided by the mesh size. For an 18 mesh screen, the next screen should be no closer than 25/18, or 1.39". This method is based on analysis that assumes that the wires are operating in the supercritical Re region[24]. The applicability of this assumption is questionable because of the low Re for the wires. In either case, using this as a minimum guide will be sufficient for our case.

Table 5 shows the spacing between the screens and other screen parameters. A common structural lumber width is 1.5"; this was used for most of the construction. The width of the first and second spacing is 1.5". Equations 7 and 8 are the formulas for the pressure loss coefficient, K, as well as the Re for the wire screen[26]. This design is easy to take apart and clean, and allows for easy screen replacement.

$$Re_{\beta} = \frac{Vd}{\beta \nu} \qquad 8\text{-}7$$

$$K = 6.5 * \frac{(1-\beta)}{\beta^2} Re_{\beta}{}^{-0.33} \qquad 8\text{-}8$$

Table 5 Summary of screen parameters

Screen #	Mesh Size (M)	Open Ratio (β)	Wire Diameter (d)	K	Re_{β}	25 M	Actual Spacing
1	18	0.704	0.009"	0.906	82	--	--
2	18	0.704	0.009"	0.906	82	1.39"	1.5" = 27 M
3	22	0.697	0.0075"	1.001	69	1.14"	1.5" = 39 M
4	26	0.65	0.0075"	1.300	74	.96"	--

8.10 Post-repair Inspection

After installation of the screens, tests were carried out to verify that the proposed modifications did successfully alleviate the problems observed. Three tests were

conducted: smoke streakline visualization, boundary layer surveys on the bottom floor and NACA 4412 pressure measurements at 8 degrees.

For the first test, streaklines were recreated in the troubled regions before the repairs. Figure 59 shows images of these new streaklines. As would normally be expected, now the streaklines follow the corners and the bottom contours very closely, and now resemble the CFD with a uniform velocity at the inlet. In addition, the center bottom streaklines no longer hits the sting balance, but remains along the wall below the measurement device.

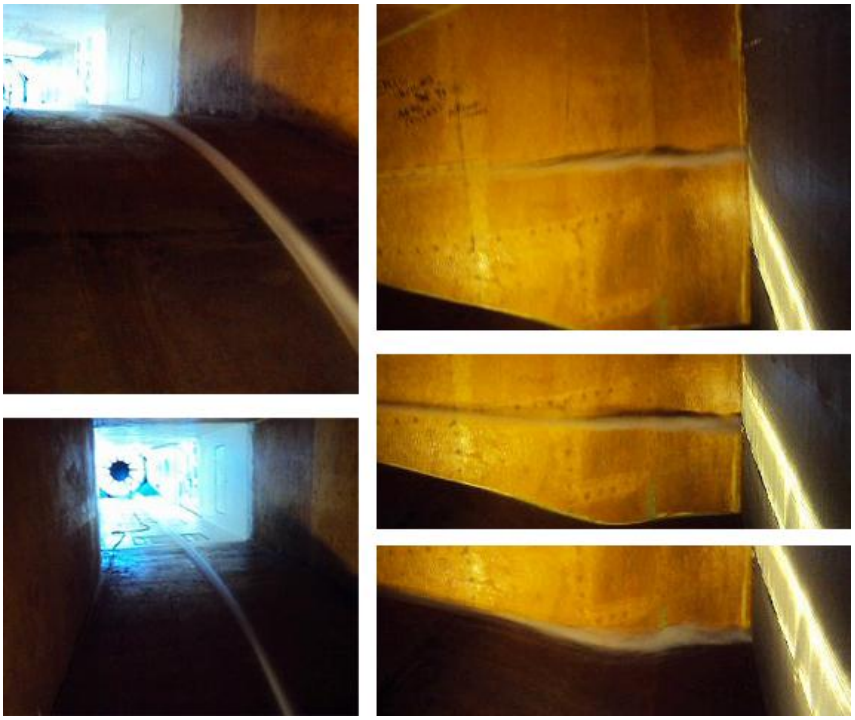

Figure 59 Streaklines after screen and honeycomb replacement

The next test carried out was a boundary layer survey of the bottom floor. Figure 60 shows the results of these measurements. After the repairs, the boundary layers showed clear profiles and steady growth along the bottom of the wind tunnel, as would be

expected. The local dynamic pressure, outside the boundary layer, showed a variance of less than 1% from the average and from the nominal freestream value over all measurements. The largest boundary layer measured was about 3 inches at a distance of about 9' from the end of the contraction. If this is the boundary layer thickness on all walls at this location then the usable tunnel area is 73% of the geometric tunnel area.

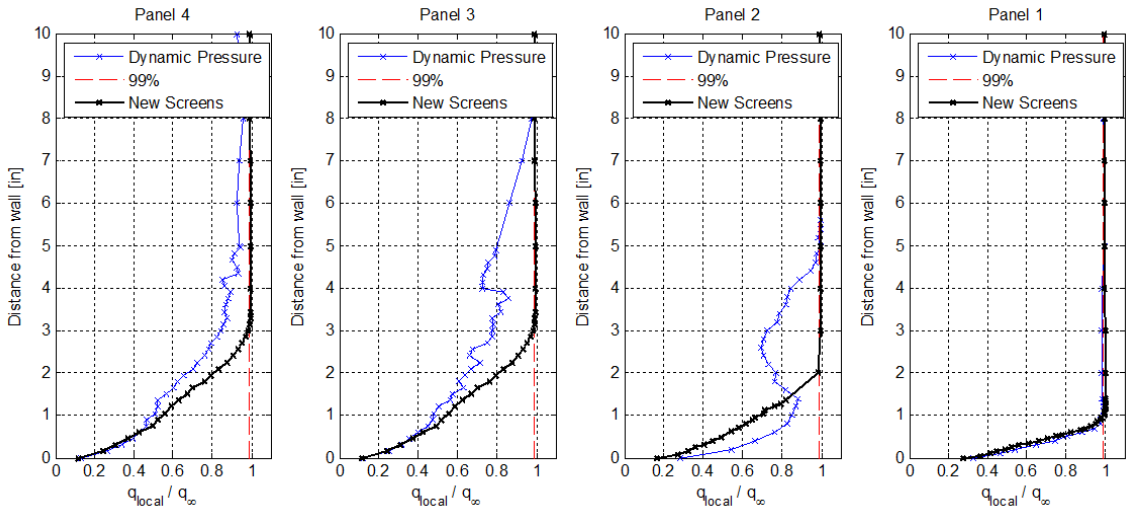

Figure 60 Boundary layer measurements before and after replacement screens and honeycomb along the floor of the wind tunnel. The panels measured from the inlet are 1', 4', 7.5', and 9' away respectively

A Pitot-static tube measured the centerline variance in dynamic pressure. Barlow et. al. recommends a variation of less than 0.5% in q[12], while Payne and The Boeing Company recommend a variance of less than 0.3% for their commercial low-speed tests[27]. The variance for the Cal Poly tunnel was measured to be 0.76%. This measurement is likely understated because long pressure tubing used during measurement often damps out pressure fluctuations. This high variance in mean dynamic pressure is likely a result of poor fan speed regulation.

The lab's cylinder was re-examined to observe the effect of the new flow quality. Sadly, it was determined that many of the problems with the cylinder are a result of poor manufacturing quality. Full 360° observation of all pressure ports showed extremely differing data sets, shown in Figure 61. It is postulated that either problems with individual pressure port installations or a warped circular profile is the cause of the problem matching theoretical distributions.

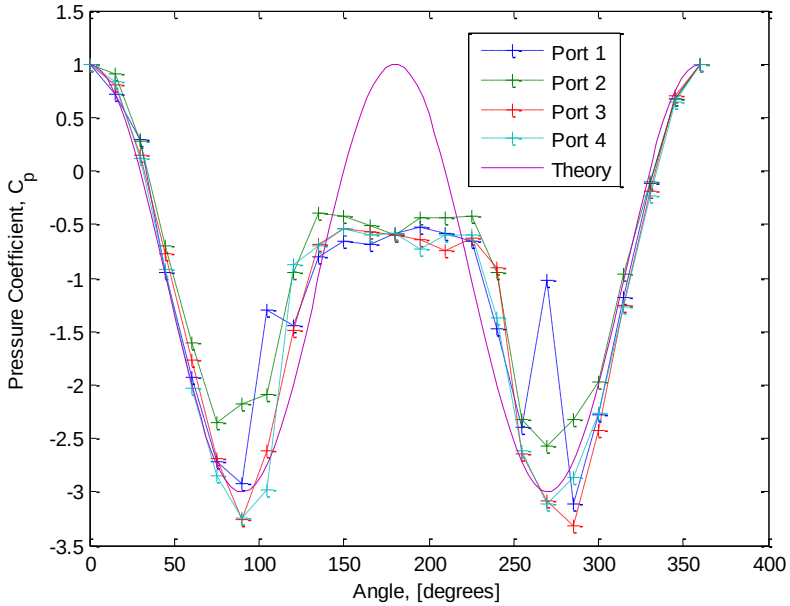

Figure 61 Cal Poly lab cylinder pressure distributions

Another test was to re-measure the pressure over the NACA 4412 to determine if the high blockage effects were eliminated. Despite positive results from other diagnostics, the new screens did not visibly change the profile over the airfoil. A more in depth study of the CFD simulation at this point would be advisable, possibly eliminating the 2-dimentional assumption. However, measurements of the boundary layers and flow visualization attest to much cleaner flow qualities after the repair.

8.11 Facility Improvement Recommendations

This study uncovered many problems of the facility as it exists today. The facility has a strong potential to serve many practical uses of the current Aerospace student body. The tunnel could be used by Design Build Fly (DBF) to obtain stability derivatives. The wind tunnel is also capable of delivering Reynolds numbers adequate for small UAVs, in which there is presently a growing interest. Yet another application could be for the current senior design class, which is currently designing a hybrid airship. Wind tunnel data would be excellent to provide when the teams get to detailed design spring quarter. All these uses, and more, are compelling reasons for improving the wind tunnel. It could become more than just an instructive tool which, in its current state, is all it is capable of being.

The first recommendation is to establish a calibration model for the lab. A symmetric, zero-lifting airplane or airfoil model on the scale of common test sizes would be ideal. This could be used to perform up-flow calibrations (by measuring lift curves for the model upright and inverted and measuring the offset) and to establish a historical database for reference. This would be extremely useful to show the repeatability of data, as well as to signify if something has gone wrong in the facility or data acquisition equipment.

The next piece of equipment the wind tunnel urgently needs is a hazardous materials cabinet stocked with flow visualization materials including kerosene, diesel, DayGlo powder, kaolin powder (China clay), various viscosity oils, and titanium dioxide. Currently, if data appears amiss, there are no established methods of flow visualization to help investigate the problem. This is an extreme disability that is relatively easy to fix.

A practice that is seriously lacking from the current operations of the wind tunnel is periodic calibration tests. This includes measuring q fluctuations, tunnel up-flow in various test sections, clear tunnel buoyance measurements, flow angularity distributions, and q distributions. These tests are vital to any facility aiming to provide repeatable, accurate data. During the current experiment, large static pressure losses were detected through different wind tunnel sections. This is a problem that could be reduced by adding fillets to the corners of the wind tunnel's rectangular cross-section.

Some of these tests could be incorporated into the AERO 307 laboratory. This would provide the double benefit of providing annually collected data for reference, as well as showing students industry practice for wind tunnels. AERO 307 students would also benefit from learning more about pressure transducers, an indispensable tool for the modern experimental aerodynamist.

Lastly, the wind tunnel lab needs some additional lab equipment. A hand-held vacuum pump is needed to perform pressure port leak tests. Scanivalve brand couplers are necessary to provide leak-free connections between pressure tubes and the Scanivalve EPS modules. Also, the lab needs the ability to provide a regulated pressure to calibrate pressure transducers for other experiments.

Figure 62 shows requirements common to commercial low speed wind tunnels. Perhaps the Cal Poly wind tunnel cannot achieve all of these requirements; however, this table outlines the metrics that should be examined.

Item	Low Speed Wind Tunnel (Closed Jet)
Total Temp., Uncertainty Total Temp., Distribution	+/- 1.0 deg. F +/- 1.0 deg. F
Turbulence, % u'/u (Outside boundary layer.)	0.05% RMS, 1Hz to 200 KHz
Static Pressure Fluctuation, p'	0.3% q_c RMS with monotonic per Hz spectra above 1000 Hz.
Max. Stream Angle	< +/- 0.1 degree
Stream Angle Gradient: ½ Span	0.008 deg/ft, chordwise near wing
Stream Angle Gradient: Full Span	0.014 deg/ft, chordwise near wing
Mach Number: Ref. Value Gradient ½ Span Gradient Full Span Cross Plane Varience	 +/-0.0004 @ M=0.3 +/-5x10^{-6} per ft @ M=0.3 +/-1x10^{-5} per ft @ M=0.3 +/- 0.0003@M=0.3
Tunnel Stability: Total & Static Pressure Total Temperature, deg F	 +/- 3 psf over 10 sec @ M=0.3 +/- 0.5° over 10 sec @ M=0.3
Total Temperature Transient	10 deg. over 10 sec.
Humidity	0.0001 lb water/lb. dry air

Figure 62 Typical flow quality requirements for a commercial low speed wind tunnel

In conclusion, laboratory data is only as accurate as the tools used to measure it. If reliable, useful wind tunnel data is desired, many of the recommended changes must be performed.

Appendix A – Complete Data

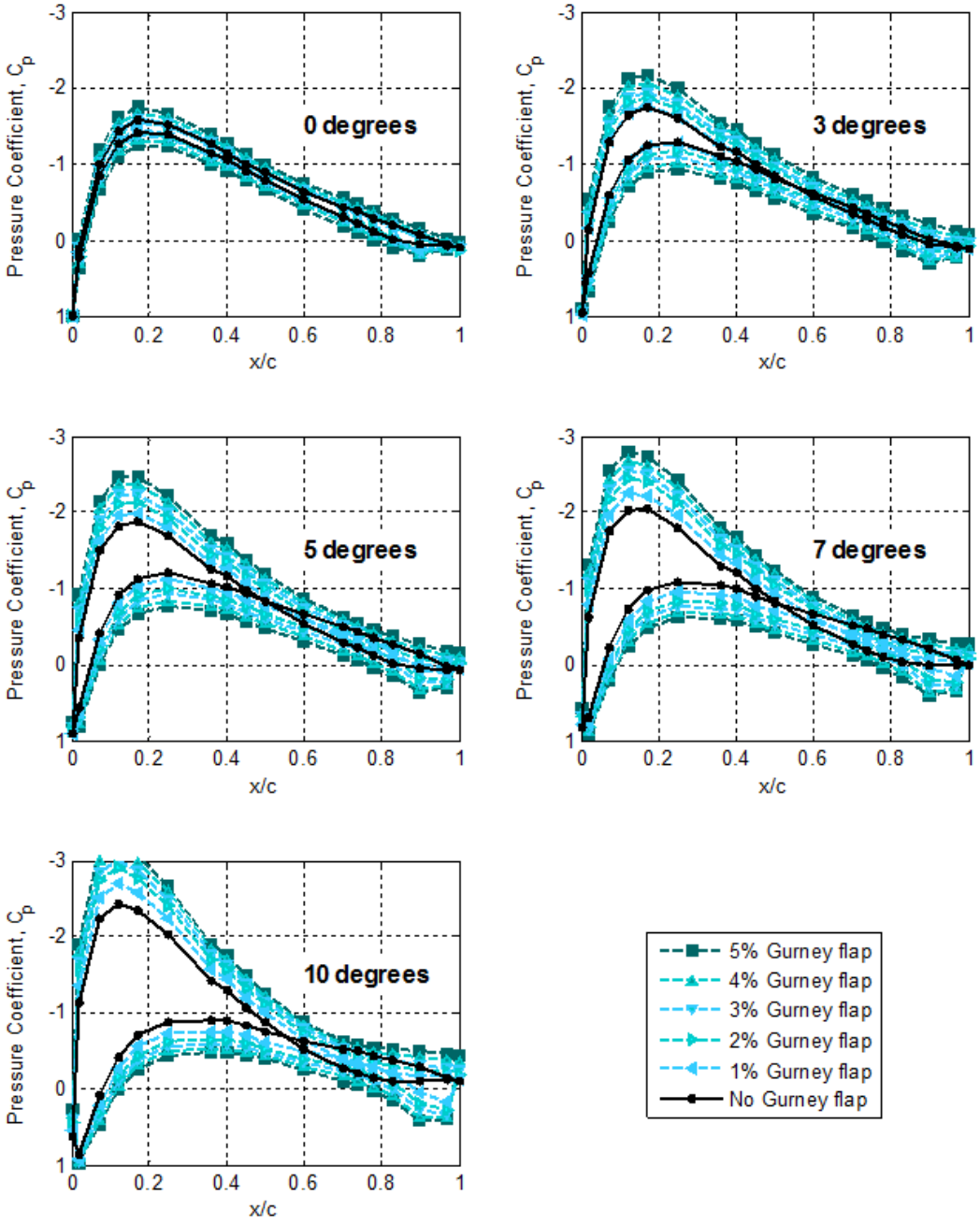

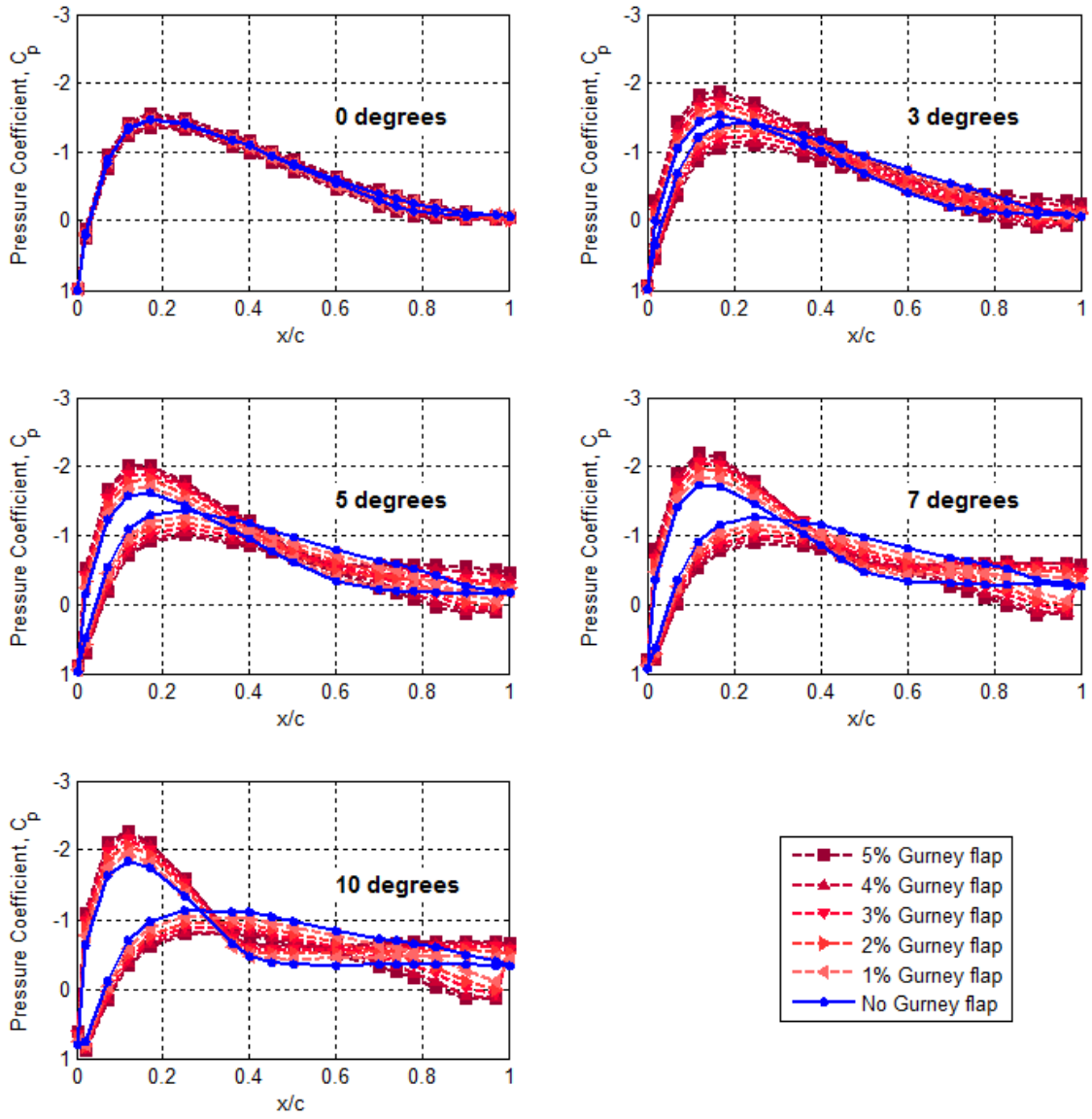
0 degrees
3 degrees
5 degrees
7 degrees
10 degrees
Pressure Coefficient, C_p
x/c
5% Gurney flap
4% Gurney flap
3% Gurney flap
2% Gurney flap
1% Gurney flap
No Gurney flap

Pressure data for negative angles of attack

Note: Data considered obsolete because it was recorded before tunnel improvements. Provided only for informative purposes

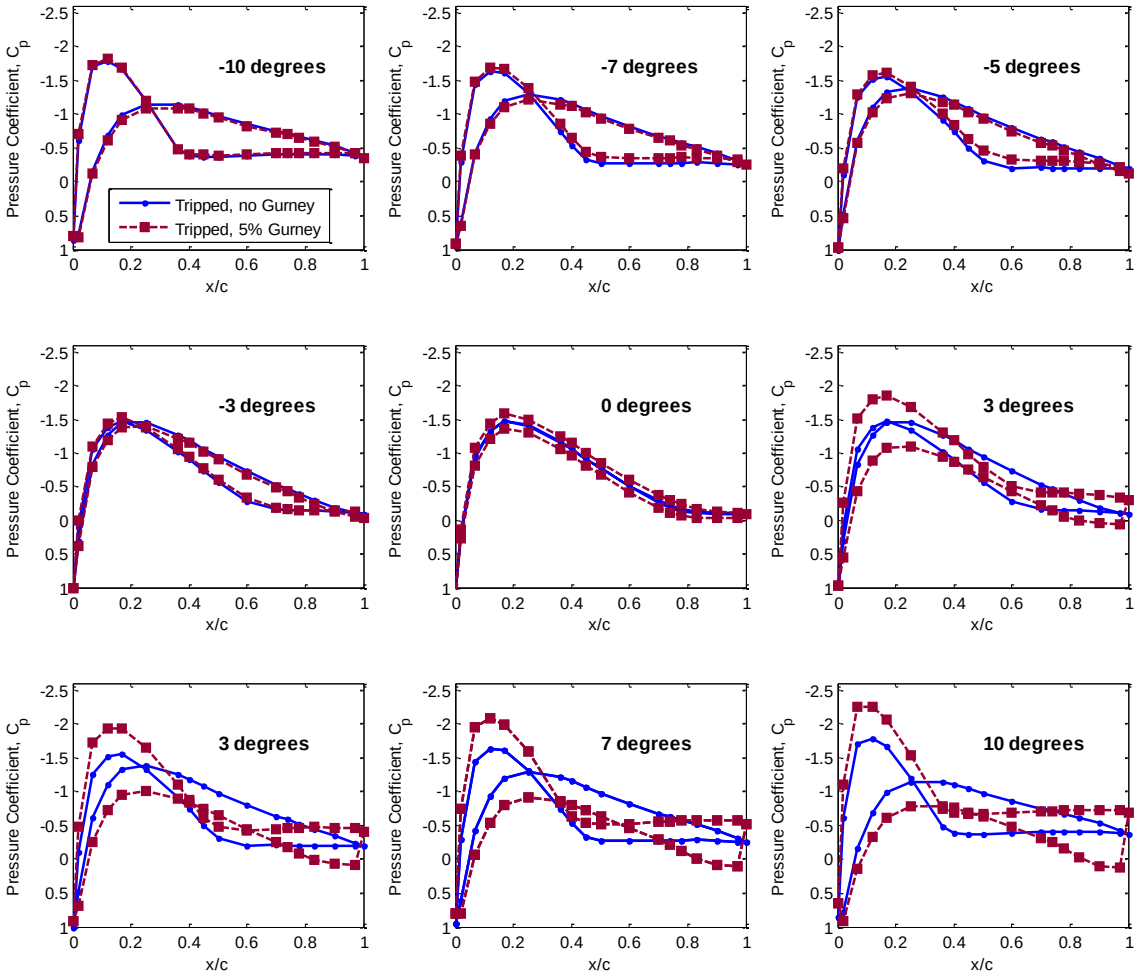

Appendix B – Probe Dimensions

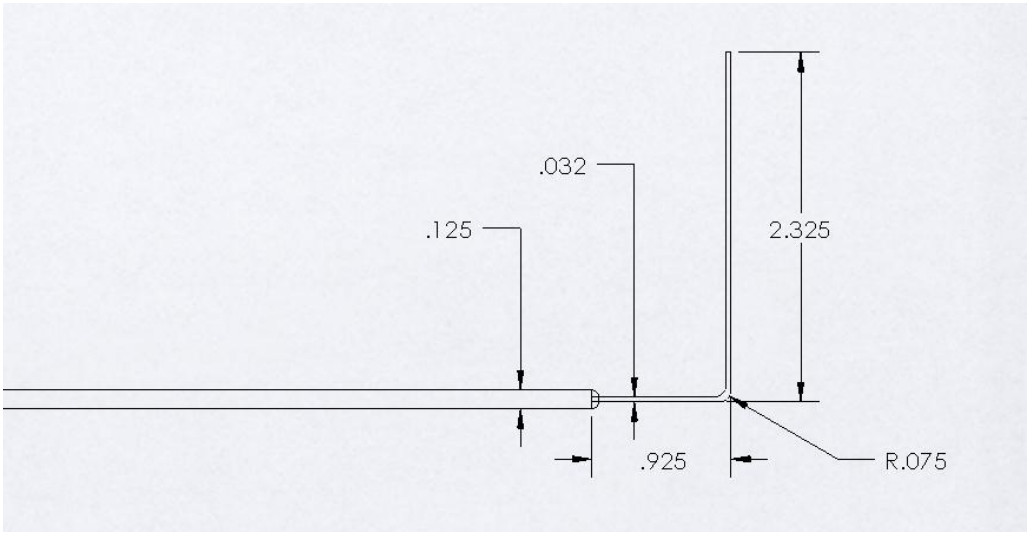

Appendix C – Tunnel Geometry

Here are the measured wind tunnel inlet 3D coordinates of the bottom corner (the intersection of the horizontal and vertical walls). These were used to model the inlet in Solidworks for the CFD study. They are probably accurate to ±1/4".

```
115.5in 84.25in 51.5in
104.75in 84.25in 51.5in
87.5in 83.5in 51in
74.75in 82.13in 50in
66.5in 80.75in 48.75in
60in 79.38in 47.5in
53.25in 77.63in 45.75in
47.13in 75.75in 43.75in
40.88in 73.13in 41.13in
32.38in 69.38in 37.25in
22.38in 63.5in 31in
16.88in 59.75in 27.38in
8.88in 53.75in 22.5in
3.88in 49.5in 20.13in
-1.5in 44.38in 18.25in
-6.12in 40.13in 17.25in
-11in 37.63in 16.63in
-16in 36.25in 16.25in
-22.25in 35.75in 16.25in
-27.37in 35.75in 16.25in
```

Appendix D – A/A_{flow} Equation Derivation

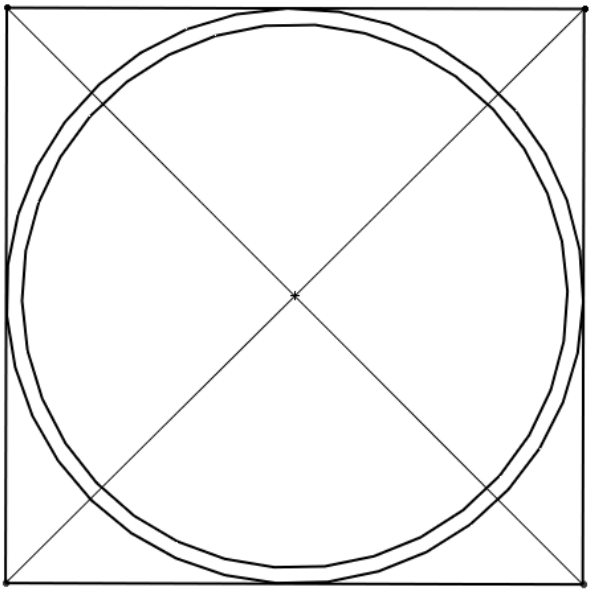

For the straws, the diameter is equal to the hydraulic diameter. It is assumed that the straws are perfect circles that touch at 4 points on their outer edge. The above figure is the domain that repeats over and over. The vertical and horizontal edges of the bounding box can be thought of as planes of symmetry or as the edges of the inlet. The derivation looks like this.

$$A = D^2$$

$$A_{straw} = \frac{\pi}{4}\left({D_o}^2 - {D_i}^2\right)$$

$$D_o = D_h$$

$$D_i = D_h - 2T$$

$$A_{straw} = \frac{\pi}{4}\left({D_h}^2 - (D_h - 2T)^2\right)$$

$$A_{straw} = \frac{\pi}{4}\left({D_h}^2 - \left({D_h}^2 - 4D_hT + 4T^2\right)\right)$$

$$A_{straw} = \frac{\pi}{4}(4D_hT - 4T^2)$$

$$A_{straw} = \pi(D_hT - T^2)$$

$$A_{flow} = A - A_{straw}$$

$$\frac{A}{A_{flow}} = \frac{D^2}{D^2 - \pi(D_hT - T^2)}$$

For the Honeycomb, the following figure was used for the analysis in the same manner as above in order to come to the relation given in the text.

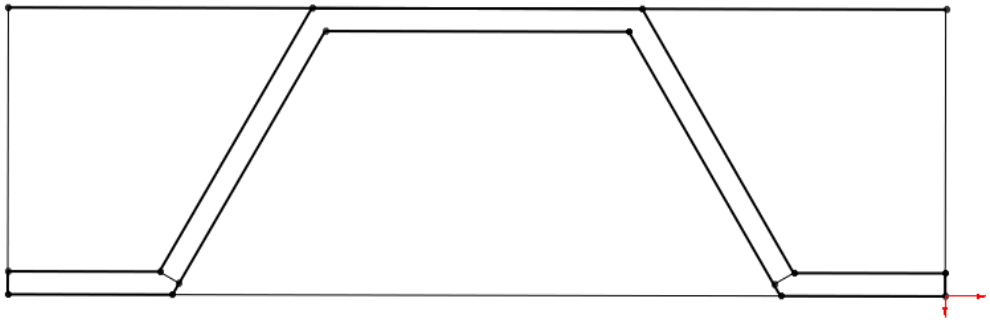

Appendix E – Matlab Code for Honeycomb Pressure Drop Coefficient

```
close all;clear all;clc
%% Inputs (some of these values need to be changed)
```

```
delta=.001;      % roughness (inches)-see "Handbook of Hydraulic
Resistance"
dh=0.125;        % hydraulic diameter in inches
L=1;             % Length of the cell in the streamwise direction in
inches
t=0.002;         % thickness of the cell walls in inches
shape='circle';  % shape of the cell (either circle or hexagon for now)

V=3.7;           % speed of the air at the entrance to the cell in m/s
nu=1.46e-5;      % kinematic viscosity in metric units

%% Preliminary Calc
dh=dh.*0.0254;
L=L.*0.0254;
delta=delta.*0.0254;
t=t.*0.0254;
Re=delta.*V./nu;

if strcmp(shape,'hexagon')==1
    A_Aflow=dh./(dh-8.*t./3);
elseif strcmp(shape,'circle')==1
    A_Aflow=dh.^2./(dh.^2-pi.*(dh*t-t.^2));
end

%% Main Calcs
if Re<=275
    lamda=0.375.*Re.^(-0.1).*(delta/dh).^.4;
else
    lamda=0.214.*delta_dh.^.4;
end
k=lamda.*(3+L/dh).*A_Aflow.^2+(A_Aflow-1).^2
```

Appendix F – Matlab Code for Panel Method

```
function [Cl Cd] = calc_coeff(CP,alpha)
%  Calculates lift and drag coefficients for a NACA 0036, giving the CP
%  vector used for plotting, and alpha in degrees

 x = [0  0.0200    0.0700    0.1200    0.1700    0.2500    0.3600
0.4000...
      0.4500    0.5000    0.6000    0.7000    0.7400    0.7800
0.8300...
      0.9000    0.9700    1.0000    0.9700    0.9000    0.8300
0.7800...
      0.7400    0.7000    0.6000    0.5000    0.4500    0.4000
0.3600...
      0.2500    0.1700    0.1200    0.0700    0.0200  0];
y = [0    0.0708    0.1226    0.1496    0.1659    0.1782    0.1778...
    0.1741    0.1674    0.1588    0.1369    0.1099    0.0979
0.0853...
```

```
    0.0685    0.0434    0.0162         0   -0.0162   -0.0434   -
0.0685...
   -0.0853   -0.0979   -0.1099   -0.1369   -0.1588   -0.1674   -
0.1741...
   -0.1778   -0.1782   -0.1659   -0.1496   -0.1226   -0.0708
0];
ref = [1 2 3 4 5 31 32 6 7 8 34 33 9 10 11 12 13 14 15 16 17 18 19 30
29 20 21 22 28 27 23 24 25 26 1];
CP = CP(ref);

%Equation for the derivative
dydx = @(x) .36/0.2*(0.2969/2*x.^-0.5-0.1260-2*0.3516*x+3*0.2843*x.^2-
4*0.1015*x.^3);
%f = @(x) .36/0.2*(0.2969*x.^0.5-0.1260*x-0.3516*x.^2+0.2843*x.^3-
0.1015*x.^4);

%Deterimines the 'm' for each panel (y=mx+b)
m = y./abs(y).*dydx(x);

%Removes NaN from first vertical panel
index = isnan(m);
m(index) = 0;

%finds b (y=mx+b)
b = y-m.*x;

%Find the endpoints for each panel
mdpt = zeros(2,length(x)-1);
for i = 1:length(mdpt)
    if i == 1
        mdpt(1,i) = 0;
        mdpt(2,i) = b(2);
    elseif i == length(mdpt)
        mdpt(1,i) = 0;
        mdpt(2,i) = b(end-1);
    elseif x(i+1) == 1
        mdpt(2,i) = .1/24;
        mdpt(1,i) = 1;
    elseif x(i) == 1
        mdpt(2,i) = -.1/24;
        mdpt(1,i) = 1;
    else
        mdpt(:,i) = [m(i) -1;m(i+1) -1]^-1*[-b(i);-b(i+1)];
    end
end



%Find the length of each panel
l = zeros(1,length(x));
gamma = zeros(1,length(x));
for i = 1:length(l)-1
    if i == 1
        l(1) = sqrt((mdpt(2,i)-mdpt(2,end)).^2+(mdpt(1,i)-
mdpt(1,end)).^2);
```

```
        gamma(i) = atan2(mdpt(2,i)-mdpt(2,end),mdpt(1,i)-mdpt(1,end));
    else
        l(i) = sqrt((mdpt(2,i)-mdpt(2,i-1)).^2+(mdpt(1,i)-mdpt(1,i-
1)).^2);
        gamma(i) = atan2(mdpt(2,i)-mdpt(2,i-1),mdpt(1,i)-mdpt(1,i-1));
    end
end


C_a = sum(l(1:end-1).*CP(1:end-1).*sin(gamma(1:end-1)));
C_n = sum(l(1:end-1).*CP(1:end-1).*-cos(gamma(1:end-1)));

Cl = C_n*cosd(alpha)-C_a*sind(alpha);
Cd = C_a*cosd(alpha)+C_n*sind(alpha);
```

References

[1] Seddon, J., Newman, S., Basic Helicopter Aerodynamics, Second Edition. AIAA Education Series, 2001, Reston, Virginia, pgs 123-4

[2] Leishman, J. Gordon, *Principles of helicopter aerodynamics*. Cambridge University Press, 2000, Cambridge, United Kingdom, pg 217.

[3] Martin, P.B., Tung, C., Arad, E. (2003) *Active Separation Control: Measurements and Computations for a NACA 0036 Airfoil*. AIAA 2003-3516.

[4] Arad, E., Marin, P. B., Wilson, J., Tung, C., *Control of Massive Separation on a Thick-Airfoil Wing: A computational and Experimental Study*. AIAA 2006-322.

[5] Wilson, J., Martin, P. B., Tung, C., *Turbulence Measurements of a Two-Dimensional NACA 0036 Airfoil with Synthetic Jet Flow Control*. AIAA 2006-3157.

[6] Huthmacher, R., *On the Effect of Boundary Layer Transition on the Massive Separation from a NACA 0036 Airfoil*. Cal Poly Master's Thesis, 2008.

[7] Hoerner, S. Borst, H. *Fluid-Dynamic Lift*. Hoerner Fluid Dynamics, 1975, pgs 2-9, 2-10.

[8] Wilson, J. *Turbulence Measurements on a 2D NACA 0036 with Synthetic Jet Flow Control* , American Helicopter Society 2006 Annual Forum, Volume 62, pp. 107-122.

[9] Schetz, J., *Boundary Layer Analysis*. Prentice-Hall, Inc. Englewood Cliffs, New Jersey, 1993.

[10] Cox, R., *Low Speed, Flat Plate, Carborundum Grit Trip Strip*. AIAA-80-0869, 1980.

[11] Braslow, Albert L., Hicks, Raymond M., Harris, Roy V. Jr., *Use of Grit-Type Boundary-Layer-Transition Trips on Wind-Tunnel Models*. NASA Technical Note, NASA TN D-3579, July 1965.

[12] Barlow, J., Rae, W. H., Pope, A., *Low-Speed Wind Tunnel Testing*, 3rd edition. John Wiles & Sons, Inc, 1999.

[13] Cebeci, T., Mosinskis, G., Smith, A., *Calculation of Separation Points in Incompressible Turbulent Flows*. Journal of Aircraft, v.9, Sept. 1972, p. 618-624.

[14] Myose, R., Papadakis, M., Heron, I., *Gurney Flap Experiments on Airfoils, Wings, and Reflection Plane Model*. Journal of Aircraft, Vol. 35, No. 2 March-April 1998, pgs 206-211.

[15] Maughmer, Mark D., Bramesfeld, Goetz. *Experimental Investigation of Gurney Flaps*. Journal of Aircraft Vol. 45, No. 6, 2008 pgs 2062-7

[16] Liebeck ,RH. *Design of subsonic airfoils for high lift*. Journal of Aircraft, 1978, p547-61

[17] Giguére, P., Lemay, J., Dumas, G., *Gurney Flap Effects and Scaling for Low-Speed Airfoils*. AIAA-95-1991-CP, 1995.

[18] Taylor, John R. *An Introduction to Error Analysis, 2nd edition*. University Science Books, 1982.

[19] Tannehil, J. C., Anderson, D. A., Pletcher, R. H., *Computational Fluid Mechanics and Heat Transfer, Second Edition*. Taylor & Francis. Philadelphia, PA, 1997.

[20] ANSYS FLUENT 6.3 Users Guide, 2006.

[21] Celik, I. B., Ghia, U., Roache, P., Freitas, C., *Procedure for Estimation and Reporting of Uncertainty Due to Discretization in CFD Application*. ASME Journal of Fluids Engineering, 1993, v. 115, pgs. 194-195.

[22] Wadcock, A. J., *Investigation of Low-Speed Turbulent Separated Flow Around Airfoils*. NASA Contractor Report No. 177450, 1987.

[23] Mehta, R.D.; Bradshaw P., *Design Rules for Small Low Speed Wind Tunnels*. The Aeronautical Journal of the Royal Aeronautical Society, November 1979

[24] Scheiman, J., *Considerations for the Installation of Honeycomb and Screens to Reduce Wind-Tunnel Turbulence*. NASA Technical Memorandum 81868. Langley Research Center

[25] Ross, J. C., *Theoretical and Experimental Study of Flow-Control Devices for Inlets of Indraft Wind Tunnels*. NASA Technical memorandum 100050. September 1989. NASA Ames Research Center, Moffet Field, CA

[26] Mehta, R.D.; Turbulent Boundary Layer Perturbed by Screens. AIAA Journal Vol 23, No. 9, September 1985, pg 1335

[27] Payne, F. M., *Low Speed Wind Tunnel Testing Facility Requirements: A Customer's Perspective*. AIAA-99-0306, 1999.